Dynamics of the Morphological Degradation of Si-Based Anodes for Li-Ion Batteries Characterized by In Situ Synchrotron X-Ray Tomography

Victor Vanpeene, Julie Villanova, Andrew King, Bernard Lestriez, Eric Maire, Lionel Roue

WILEY-VCH

DOI: 10.1002/ ((please add manuscript number))
Article type: Full Paper

Dynamics of the morphological degradation of Si-based anodes for Li-ion batteries characterized by *in-situ* synchrotron X-ray tomography

Victor Vanpeene, Julie Villanova, Andrew King, Bernard Lestriez, Eric Maire and Lionel Roué**

V. Vanpeene, Prof. L. Roué
Institut National de la Recherche Scientifique (INRS)
Centre Énergie, Matériaux, Télécommunications (EMT)
1650, boulevard Lionel Boulet
Varennes (QC) Canada J3X1S2
E-mail : Lionel.Roue@emt.inrs.ca

Dr. J. Villanova
ESRF-The European Synchrotron, ID16B,
F-38000 Grenoble, France

Dr. A. King
Synchrotron Soleil, Psiché beamline,
F-91190 Gif-sur-Yvette, France

Dr. B. Lestriez
Institut des Matériaux Jean Rouxel (IMN)
CNRS UMR 6502
Université de Nantes
F-44322 Nantes Cedex 3, France

V. Vanpeene, Dr. E. Maire
INSA Lyon
MATEIS
CNRS UMR 5510
F-69621 Villeurbanne, France
E-mail : eric.maire@insa-lyon.fr

Keywords: lithium-ion battery, silicon anode, X-ray tomography, morphological dynamic

Abstract

The alloying reaction of silicon with lithium in negative electrodes for lithium-ion batteries causes brutal morphological changes that severely degrade their cyclability. In this study, the dynamics of their expansion and contraction, of their cracking in the bulk and of their debonding at the interface with the current collector are visualized by *in-situ* synchrotron X-ray computed tomography and quantified from appropriate 3D imaging analyses. Two electrodes made with same silicon material having reasonable particle size distribution from applied point of view are compared: one fabricated according to a standard process and the other one prepared with a maturation step, which consists in storing the electrode in a humid atmosphere for a few days before drying and cell assembly. All morphological degradations are significantly restrained for the matured electrode, confirming the great efficiency of this maturation step to produce a more ductile and resilient electrode architecture, which is at the origin of the major improvement in their cyclability.

1. Introduction

Because increasing the energy density of lithium-ion batteries is still a challenge especially for electric vehicle application, different anode materials with high theoretical capacities have been investigated.[1,2] Among them, silicon has drawn a lot of attention due to its gravimetric capacity ten times higher than graphite (3579 mAh g^{-1} for $Li_{15}Si_4$ *versus* 372 mAh g^{-1} for LiC_6). Si is also earth-abundant, low-cost and non-toxic. However, its use in commercial Li-ion batteries is challenging because the capacity retention and coulombic efficiency of Si electrodes are much lower than for graphite electrodes.[3,4] This is related to the important volume change of Si during its lithiation (up to 280% for $Li_{15}Si_4$ *versus* ~10% for LiC_6), which deteriorates the electrode architecture, and destabilizes the solid electrolyte interphase (SEI). The optimization of the mechanical properties of Si-based electrodes is thus

a key issue to improve their electrochemical performances. This optimization must be done at the Si particle scale as well as at the composite electrode scale.

The use of nanosized Si materials (nanoparticles, nanowires, nanopillars, nanocomposites) has demonstrated a great efficiency for limiting the pulverization of the Si active material upon cycling as its fracturing resistance is size-dependent.[5] One must however note that the synthesis of such nanosized materials at industrial scale and competitive cost remains an issue, in addition to their low tap density and high surface reactivity. It thus appears more relevant to use micrometric particles, *e.g.* ball-milled nanocrystalline/amorphous Si[6] or nanostructured Si alloys[1,7] able to prevent the formation of crystalline $Li_{15}Si_4$, which is known to promote particle fracture due to its large phase boundary stress with amorphous Li_xSi during delithiation.

The mechanical properties (compliance) of the SEI layer must also be optimized to be able to tolerate the large volume variation of the Si particles. To date, the use of appropriate electrolytes or electrolyte additives such as fluoroethylene carbonate (FEC)[8] appears as the most judicious strategy.[9] However, this interfacial issue is still not fully resolved and is probably the most important obstacle for the implementation of Si-rich based anodes in commercial Li-ion batteries.

At a larger spatial scale, the volume change of the electrode is likely to induce its macrocracking, collapsing and/or delamination from the current collector, leading to electrical disconnection of some Si particles.[10] In order to limit these morphological degradations, the cohesion and adhesion strength of the Si electrodes needs to be improved. These have been shown to be highly dependent on the nature of the electrode binder.[7,11] The crucial role of the polymer binder has been brought to light by early studies aiming at comparing the performance of the commonly used polyvinylidene difluoride (PVDF) with those of alternative binders, such as carboxymethylcellulose (CMC).[12,13] It was shown that the chemical interaction of the CMC binder with the Si particles is responsible of its efficiency

rather than its physical properties (flexibility).[13] This chemical bonding results from the condensation reaction between -OH groups present at the surface of the Si particles and -COOH groups of CMC, which is favoured using a buffered pH3 slurry media.[14] Since these observations, various functionalized and water-soluble binders have been investigated and some of them have shown promising performances for Si-based electrodes.[15,16] Note that these binders can also act as protective SEI layer, improving the initial coulombic efficiency.[17]

It was also shown that the efficiency of acidic aqueous binders can be greatly enhanced through a post-processing treatment (called maturation) consisting of storing the Si-based electrode in a humid atmosphere for a few days before drying and cell assembly.[18] During this maturation step, the binder tends to concentrate at the silicon interparticle contacts, which improves the cohesion strength of the electrode. At the same time, the corrosion of the copper current collector induces the formation of copper carboxylate bonds, improving the adhesion strength the electrode onto the current collector. The result is a significant electrochemical performance gain, up to a factor 10, compared to a standard (not-matured) electrode. This maturation procedure can also restore bonds that are broken during the calendering process, resulting in substantially improved cycling capability of calendered electrodes.[19]

A better comprehension of the morphological changes of the Si-based anodes with cycling, which occur at different scales (*i.e.* from the Si particle to the global electrode architecture as previously argued), requires powerful analytical tools. X-ray computed tomography (XRCT) is relevant for this purpose due to its ability to characterize complex structures in 3D. As listed in **Table S1** (Supporting Information), this technique has been used for *in-situ*[20-30] and *ex-situ*[31-33] studies on various Si-based electrodes, with a reconstructed volume ranging from ~10^{-3} mm^3 [31] to ~10 mm^3 [20] and a voxel size ranging from 0.06 µm[31] to 9.3 µm[20] (the spatial resolution corresponds to about two times the voxel size). Relevant information on the electrode degradation process have been obtained such as its

delamination[20], the Si particle cracking[21,25] and disconnections[23], the morphological evolution and connectivity of the pores and solid phases.[24,26,28] However, it must be noted that most of these XRCT studies have been performed on thick electrodes made with large Si particles (typically ≥ 20 μm in diam.), which are not very representative of a real electrode. Moreover, these previous studies are mainly focused on qualitative analyses.

In the present study, *in-situ* synchrotron XRCT characterization technique is implemented to monitor the morphological evolution with cycling of Si-based electrodes made with micrometric Si particles (d_{50} = 2.5 μm). The behaviour of two electrodes is compared: one prepared using a standard procedure and the other one prepared with a maturation step.[18] Various morphological parameters are quantified and followed during the 1st cycle, namely *(i)* the dimensional change of the electrode, *(ii)* the volume fraction, size and connectivity of the segmented solid, gas and electrolyte phases, *(iii)* the volume fraction, size and connectivity of the produced macrocracks, *(iv)* the surface area of the produced delaminated zones from the current collector and *(v)* the variation of the Si inter-particle distances. For the first time, the dynamics of the electrode macrocracking and delamination is clearly evidenced from *in-situ* qualitative and quantitative 3D imaging analyses. These morphological degradations are much less intense for the matured electrode, confirming the efficiency of the maturation procedure to enhance the mechanical strength of the Si-based electrodes.

2. Results and discussion

Both standard and matured electrodes have the same composition, namely 73.1%^{wt} of ball-milled silicon (d_{50} = 2.5 μm) as active material, 11.0%^{wt} of graphene nanoplatelets (GnP) as conductive additive, 7.3%^{wt} of carboxymethylcellulose (CMC) as binder, and 7.7%^{wt} of citric acid and 0.9%^{wt} of KOH salts originating from the pH3 buffered slurry solution. Their

active mass loading is 5.5 mg $_{Si}$ cm^{-2} and their pristine thickness is ~95 µm. Details on the electrode preparation and the maturation procedure are given in the Experimental section.

In-situ synchrotron XRCT measurements were performed during the 1st cycle on both electrodes using an X-ray compatible electrochemical cell (see **Figure S1a**, Supporting Information). The total imaged volume for the standard electrode is 1333×1333×210 µm^3 with a voxel size of 650 nm (see **Figure S1b**, Supporting Information), and 256×256×210 µm^3 with a voxel size of 200 nm for the matured electrode (see **Figure S1c,** Supporting Information). This difference is due to the fact that XRCT experiments were performed using two different synchrotron facilities: Soleil synchrotron for the standard electrode and ESRF synchrotron for the matured electrode (see the Experimental section for more detail). This is because the amount of beam time allocated on each beam-line was too short to perform both experiments at the same place. Nevertheless, the resolution change is not affecting our main conclusions, as the morphological changes analysed on both electrodes have dimensions higher than 600 nm. Moreover, both electrodes are compared from an identical reconstructed volume of 190×190×210 µm^3. Such a volume can be considered as representative of the whole electrode volume (see **Figure S2** and related comments, Supporting Information).

Using appropriate image processing, segmentation and analysis procedures as described in the Experimental section and Supporting Information, various morphological parameters of different identified domains and their evolution during the 1st cycle have been quantified and compared for both electrodes as presented hereafter. These parameters are listed in **Table 1** for the pristine state, after the 1st discharge and after the 1st charge. The evolution during the first cycle of some key morphological features for both electrodes, namely their thickness expansion/contraction, the volume fraction of macrocracks, the coating / current collector delamination area and the mean Si interparticle distance variation are collected in **Figure 1**.

2.1. Pristine state

At the pristine state, both electrodes have a similar porosity of about 38-39% (**Table 1**). Only 2-3 % of the pores contain gas (*i.e.* are electrolyte-free), confirming their nearly complete impregnation by the electrolyte. The median diameter of the pores is lower for the matured electrode (d_{50} = 2.6 µm) than for the standard one (d_{50} = 5.4 µm). This difference may partly result from the higher XRCT resolution for the matured electrode, permitting a better identification (segmentation) of the smallest pores. Note that the electrode porosities measured here may be underestimated as the reconstructed volumes do not permit the identification (segmentation) of the electrolyte phase located in the submicrometric interstices of the composite solid phase due to resolution limitation. The homogeneous distributions of the electrolyte-filled pores and solid phase in the electrodes are highlighted by their high intra-connectivity (about 98 and 100%, respectively). Here, all the solid components of the electrodes (*i.e.* Si particles, GnP conductive additive, CMC binder and CA/KOH salts) are considered as a unique domain labelled "solid phase" since they cannot be precisely differentiated due to their similar attenuation coefficient and/or too small size. Actually, only a few large Si particles can be clearly identified in the solid phase (see 3D views of the pristine standard and matured electrodes in **Figure S3**, Supporting Information). As expected, no macrocrack in the bulk of the electrodes and no significant delaminated zone at the electrode/current collector interface are detected at the pristine state.

2.2. Electrochemical behavior

The potential evolution during the 1st cycle of the standard and matured electrodes is presented in **Figure 1a** and **1b**, respectively. The potential jumps correspond to XRCT acquisition steps where the cell was let to the open circuit potential. The electrochemical cells were galvanostatically discharged and charged between 1 and 0.005 V *vs* Li/Li$^+$. The applied current was 180 mA g^{-1} of Si (C/20) for the standard electrode. A higher current of 600 mA g^{-1} Si (C/6) was applied for the matured electrode, as only one day of beam time was allocated

for this experiment. A first discharge (charge) capacity of 1311 (734) mAh g^{-1} of Si, corresponding to an initial coulombic efficiency (CE) of 56.0%, are obtained for the standard electrode. For the matured electrode and despite its higher C-rate inducing a larger polarization, those values are better, respectively 1801 (1088) mAh g^{-1} and 60.4%. This already highlights positive impact of the maturation on the electrode performance. Note that the observed capacities are much less than the theoretical capacity of Si for both electrodes and are about 2 times lower than those previously observed with a lower areal mass loading of 1-2 mg $_{Si}$ cm^{-2}. [18] Actually, this can be mainly explained by the fact that the Si particles are not fully lithiated when the present electrodes reach the discharge cut-off potential due to their high polarisation resistance resulting from their high mass loading (5.5 mg $_{Si}$ cm^{-2}). Indeed, it is well known that the resistance to the electronic and ionic charge transport through the composite electrode increases with the electrode loading (thickness) as the lengths of the electronic and ionic paths increase with the electrode thickness.[34]

2.3. Electrode volume (thickness) variation

The dimensional changes of the electrode mainly occur in the vertical direction (electrode thickness) thanks to the flexibility of the separator whereas the in-plane expansion is constrained by the fixed dimensions of the Cu substrate. This is highlighted in **Figure S4** (Supporting Information) which shows the relative dimensional change of both electrodes along the three Cartesian axes.

Figure 1c shows the relative variation of the electrode thickness during the 1st cycle for the standard and matured electrodes. The theoretical variation in thickness assuming no change in percent porosity is also shown for comparison (dotted lines). This one is higher for the matured electrode due to its higher capacity as shown in **Figures 1a-b**. Details on the theoretical calculation are presented in Supporting Information. The experimental thickness variation is lower for the matured electrode despite its higher discharge capacity with a

maximal expansion of 48% compared to 72% for the standard electrode. Moreover, the observed slope in thickness change is lower than the theoretical slope for the matured electrode, suggesting that its porosity is able to partially buffer the Si expansion in contrast to the standard electrode. This indicates that in the standard electrode the contacts between the Si particles are more rigid and non-slippery. Each particle expands, repels its neighbors and the porosity contained in the interstices between them increases at the same time. On the contrary, for the matured electrode, the contacts between the particles would be slippery, allowing the sliding of the particles and their displacement in the open spaces (porosity). This is consistent with a plastic behaviour in the case of the matured electrode, and a more fragile behaviour in the case of the standard electrode, accentuating its macrocracking upon charge as discussed below. Additionally, an abrupt increase in thickness is observed at a depth-of-discharge (DOD) of ~70% for the standard electrode. This can be correlated to the increase of the electrode delamination observed at the same discharge period (**Figure 1e)**. This event also induces a potential drop as seen in **Figure 1a**, reflecting an increase of the polarisation resistance since this delamination must induce the rupture of the electrical network in the electrode. For both electrodes, a residual thickness expansion is observed at the end of the charge (25 and 21% for the standard and matured electrode, respectively). This indicates irreversible change in the electrode architecture. The incomplete delithiation (deflation) of some Si particles due to their electrical disconnection can contribute to this irreversible deformation.

2.4. Electrode macrocracking

The microcracks, likely to occur at the Si particle level[21,25], is not quantified here due to resolution limitation. **Figure 1d** shows the evolution of the volume fraction of macrocracks formed in the standard and matured electrodes. For both electrodes, the formation of macrocracks is only observed during the delithiation. This cracking is much more intense for

the standard electrode, especially from a SOC of about 75% where an abrupt increase of the volume fraction of cracks can be observed. After the first delithiation, the amount of cracks reaches 11.6% and 3.5% for the standard and matured electrode, respectively.

As shown on the transversal and lateral XRCT images of the electrodes at the end of the 1st charge (**Figure 2a-d**), not only the amount but also the size (width) of the macrocracks are larger for the standard electrode. This is confirmed from their respective thickness distribution shown in **Figure 4c**, which indicates a median crack width of 13.1 μm for the standard electrode *versus* 4.8 μm for the matured electrode. The cracks are filled with electrolyte (in dark grey) or gas (in black). The fraction of gas-filled cracks seems to be larger for the standard electrode. Actually, the amount of cracks filled with electrolyte is close to ~2%^{v} in both cases, but the proportion of cracks filled with gas is five times higher for the standard electrode (**Figure 4d**). This difference can be explained by considering that the wider cracks in the standard electrode should lower the interfacial capillary forces. The density of cracks seems to be higher near the current collector (at z_3 ~15 μm). It is also possible to observe some large cracks going through the entire electrode thickness on the transversal image of the standard electrode and splitting the electrode along islands of several hundreds of microns in width, as seen in the lateral images of the standard electrode (**Figure 2 b-d**). These XRCT observations are in accordance with the morphological observations obtained at a larger scale by *operando* optical microscopy.[18]

Complementary to these analyses, it has been possible to follow the crack growth dynamics in the electrodes from 3D imaging acquired along the 1st charge. **Figure 3a-b** shows 3D views of the standard and matured electrodes at different state-of-charges (SOC) where newly formed cracks at a given SOC are in red and those previously formed are in grey. For clarity considerations, lateral *(x,y)* images corresponding to the dashed blue plane in the 3D views are also displayed. The dynamics of the electrode macrocracking is also highlighted

from the XRCT movies (see **video 1** for the standard electrode and **video 2** for the matured electrode, Supporting Information).

For the standard electrode (**Figure 3a**), the first cracks (0.8%^{v}) are formed at 30% SOC. One major crack is formed near the current collector interface and is highly oriented along the electrode thickness (*z* axis). The other one is smaller and forms at a higher *z* position with the same orientation. While reaching 43% SOC, the length of these two cracks have increased in the direction perpendicular to the current collector. Also a new crack is formed at a higher *z* position in the electrode, doubling the total volume fraction of crack at this step (1.6%). From this step and until 71% of SOC, the three main cracks are growing mostly in the *x,y* directions. From 71 to 85% SOC, there is coalescence of the earlier cracks and formation of new cracks and thus the volume fraction of cracks and their intra-connectivity are drastically increased respectively from 2.0% to ~7.9% and from 45% to 90%. The initial isolated cracks clearly coalesce into a single fully connected macrocrack. This is particularly visible on the *(x,y)* lateral images. This might be due to the sudden breakage of the already weakened binding bounds of the composite structure at this moment. During the next charge steps and until the end of the charge, the crack growth continues (up to 11.6%^{v}) but in a more progressive way and mostly in the *x,y* lateral directions. Noteworthy, although the higher contraction occurs along the *z* axis during delithiation (see **Figure S4**, Supporting Information), the cracks are all formed parallel to this *z* axis in the standard electrode. This can seem paradoxical from a mechanical point of view. To explain this, we believe that cracking during contraction is due to the constraint imposed by the current collector in the *x* and *y* directions. In these two directions, the electrode is strongly contracting but the collector is not. This leads to large deformation incompatibilities in the *x* and *y* directions while nothing constrains the electrode in the *z* direction. This is the reason why the cracks are occurring in planes perpendicular to *x* and *y*. This process is commonly known as "mud cracking" occurring when there is a biaxial

stress in the film, which fractures into a series of islands similar to that seen in areas of drying mud. [35]

In comparison, for the matured electrode (**Figure 3b**), the crack growth is more progressive and much less important. The cracks are randomly spread in the electrode volume with a low volume fraction and intra-connectivity. At the end of the charge, the volume fraction of macrocracks is only 3.5% with an intra-connectivity of 32%. One big single crack is observed in the diagonal of the observed region. The difference in the cracking pattern is highlighted in **Figure 4a-b,** which compares 3D views of the cracks formed for the standard (a) and matured (b) electrodes at the end of the 1st cycle. The largest intra-connected crack cluster is in green and the second one in blue on these 3D images. For the standard electrode, most of the volume of cracks is included in the largest interconnected cluster (74.5%), as the second one is counting for only 1.3%. In comparison, the cracks in the matured electrode form different clusters. The largest one represents 31.8% of the total crack volume. This crack is going through the entire analysed lateral dimension (~190 μm) but is limited along the thickness direction of the electrode (~45 μm) in contrast to the cracks of the standard electrode which cross all the electrode thickness (~130 μm). This could be explained by more compliant anchoring of the matured electrode to the current collector compared to the standard electrode, buffering the contraction incompatibility between the electrode and the collector and thus avoiding cracks initiating from this interface. Moreover, from a basic mechanical point of view, a crack is expected to propagate through a deformed material if the elastic energy released by the crack growth is greater than the energy required to create the fractured surfaces. [36] In other words, the mechanical energy of deformation associated with the contraction of the electrodes can be either released by macrocracking or/and dissipated by a combination of viscoelastic and plastic processes. The four times higher volume fraction of cracks in the standard electrode indicates that the polymeric binding network is more likely to

release energy by cracking in this case, which is indicative of a more fragile behaviour of the composite electrode. Therefore, according to basic mechanics, it can be said that maturation changes the fragile mechanical property of the electrode to a more ductile one, which must be related to a significant modification of the binder phase mechanical properties. [37]

2.4. Electrode delamination from the current collector

Figure 5a-b presents *(x,y)* lateral images acquired at the electrode/current collector interface for the (a) standard and (b) matured electrodes at the initial state and for different DOD and SOC values. The delaminated areas are enlightened in red on the corresponding images. Here the entire imaged *(x,y)* lateral section of the electrodes is shown. Note that the black circle observed on some images of the standard electrode (at DOD 100%, SOC 30%, SOC 75%) corresponds to a ring artefact probably enhanced by the presence of the highly absorbent copper collector nearby.[38] It appears clearly from these images that the delamination of the Si-based coating from the Cu current collector is very limited for the matured electrode compared to the standard one. This is also visible in the corresponding XRCT movies, highlighting the dynamics of the electrode delamination process (see **Video 3** for the standard electrode and **Video 4** for the matured electrode, Supporting Information). The quantification of their relative delaminated area with cycling is presented in **Figure 1e**. For the standard electrode, a significant and linear increase of the delaminated area is observed from 25% DOD. An abrupt increase is observed at ~70% DOD, which can be correlated to the abrupt increase of the electrode thickness (**Figure 1c**) and to the potential drop (**Figure 1a**) as previously discussed. At the end of the 1st discharge, the delaminated area reaches a maximal value of 17.4%. In comparison, no significant delamination is observed for the matured electrode. During the charge, the delamination area of the standard electrode is firstly reduced until reaching 50% SOC. This can be explained by the deformation of the electrode during shrinkage, restoring some contact with the current collector. This is

supported by transversal *(x,z)* images of the standard electrode where partial restoration of the film/Cu substrate contact is discernible during the charge (see **Figure S5a**, Supporting Information). From ~50% SOC, the delamination area of the matured electrode increases again in accordance with the accentuation of its macrocracking (**Figure 1d**) which preferentially initiates from the film/current collector interface as previously argued. As shown in **Figure 1e**, for the matured electrode, an increase of the delamination area is observed during the charge to reach a maximum value of 1.6%, which is 8 times lower compared to the standard electrode (12.5%), confirming again its stronger adherence to the current collector. This can be explained by the formation of copper-carboxylate coordination bonds between the Cu current collector and the CMC binder, as a result of the atmosphere-induced corrosion of copper activated by the acidic functional groups of the binder during the maturation step.[18]

2.5. Silicon particle tracking

The tracking of three selected Si particles, sufficiently large to be discernible (segmented) in the solid phase, was performed along the 1st cycle for the standard and matured electrodes. **Figure 6a** and **6b** shows lateral*(x,y)* images of 20×20 µm^2 focused on one of these Si particles (~10 µm diam.) along the 1st cycle for the standard and matured electrodes, respectively. The equivalent images for the particles #2 and #3 are shown in **Figure S6a-b** (Supporting Information). For both electrodes, the large Si particle, initially well discernible, becomes increasingly greyish as the discharge progresses since its mean attenuation coefficient is reduced proportionally to its density, which decreases as its lithiation level increases. On can note that the surrounding smaller Si particles observed in **Figure 6a** seem to be fully lithiated earlier as they "vanish" at ~70% DOD whereas the large Si particle is still visible. In addition, for the standard electrode at 45% DOD, some pores initially filled

with electrolyte become gas-filled. This indicates that the gas, present in the pristine electrode (2.1%^{v}, **Table 1**) or likely to be produced during the SEI formation[22,28], can move freely through the global porous network of the electrode. At 100% DOD, the large Si particle is nearly no longer distinguishable from its surrounding matrix (because highly lithiated) for both electrodes. During the charge of the standard electrode, the formation of a gas-filled macrocrack (in black) can be observed, which enlarges as the SOC increases. In comparison, no macrocracks are observed for the matured electrode (see **Figure 6b** and **S6b**). Note that for both electrodes, no microcracking of the Si particles is detected here despite their large size. If any, the opening of these microcracks, lower than the present XRCT resolution, may prevent their detection. Furthermore, it should be considered that the poorly crystallized state of the Si particles at the initial state (63% amorphous) is likely to limit their fracturing by favoring a more homogeneous deformation of the Si particles during their lithiation.[39,40] On the other hand, it is noticeable that the silicon particles do not recover their initial bright aspect at the end of the charge, which may indicate that their lithiation is not fully reversible. In addition, they do not recover their initial position, reflecting irreversible change in the electrode architecture.

In order to quantify the distortion of the silicon particle network along cycling, the interparticle distances $d_{1\text{-}3}$ (between particles #1 and #3), $d_{1\text{-}2}$ (between particles #1 and #2), $d_{2\text{-}3}$ (between particles #2 and #3) have been measured along the 1st cycle for both electrodes. These distances are typically around 100±50 µm. Their respective relative evolution with cycling can be found in **Figure S7** (Supporting Information). The evolution of the Si inter-particle distance (expressed in relative variation) averaged from the displacements of the 3 particles is presented in **Figure 1f** for the standard and matured electrodes. The difference is strikingly visible between both electrodes. In fact, the variation of the inter-particle distance is much larger, less progressive and less reversible for the standard electrode. Maximum variations of 57 and 9% are reached at the end of the discharge and irreversible variations of

19 and 1% are observed at the end of the charge for the standard electrode and matured electrode, respectively. This confirms the higher cohesion strength of the binding matrix of the matured electrode[18], which limits variation in the electrode thickness associated with the volume expansion/contraction of the Si particles. These results obtained at the Si particle scale are in accordance with the volumetric (thickness) variations measured at the composite electrode scale (**Figure 1c**). By comparing **Figure 1f** and **1c**, one can however note some differences with lower and more reversible variations of the Si particle network compared to the electrode thickness for the matured electrode and more abrupt (less linear) variations at the Si particle network compared to the electrode thickness for the standard electrode. This can be explained by the fact that the relative distance variation between different expanding areas of the matured electrode are lowered compared to the standard electrode, due its more anisotropic expansion. This suggest that the matured electrode has a predisposition for maintaining the Si inter-particle distance while the entire volume of the electrode is expanding, meaning that the different parts of the electrode are expanding at the same rate.

2.6. Variation of the electrolyte volume

During the discharge, electrolyte will be drawn into the negative electrode due to its volume expansion and will starve the rest of the cell of electrolyte. Additionally, some electrolyte will be consumed through the SEI formation. An excess of electrolyte is thus required in the cell to accommodate these effects.

The relative variation of the electrolyte volume in the anode during the 1st discharge is shown in **Figure 7**. It was established from the acquired XRCT images, in which the electrolyte phase can be segmented and quantified as detailed in Supporting Information. For the standard electrode (black curve), a sudden drop of ~30% of the electrolyte volume is observed during the initial stage of the discharge, which can be explained by the electrolyte consumption due to the SEI formation. From a DOD of 10%, the volume of electrolyte in the

electrode is gradually increasing as the electrode volume expands to reach ~20% at the end of the 1st discharge. A similar behavior is observed for the matured electrode (blue curve) but the relative variation of the electrolyte volume is less marked, which is in accordance with the lower thickness expansion of the electrode observed in **Figure 1c**. Based on these data, one can estimate the excess of electrolyte required in a cell at 200 and 80 µL per cm^3 of anode (with an electrolyte-filled porosity of ~36% at the pristine state) for the standard and matured electrode, respectively. These values should differ with calendered (less porous) electrodes.

3. Conclusion

This study has highlighted the ability of the X-ray computed tomography for imaging and quantifying morphological dynamics of Si-based anodes for Li-ion batteries. From these analyses, it has been demonstrated the great efficiency of a post-processing maturation treatment for *(i)* limiting the macroscopic deformation (expansion/contraction) of the electrode, *(ii)* decreasing the formation of macrocracks in the composite electrode; *(iii)* preventing its delamination from the current collector and *(iv)* constraining the displacement of the Si particles during the discharge and charge of the electrode. All these observations support the fact that the maturation process brings considerable improvement in the cohesion and adhesion strengths of the Si-based electrode, inducing major gain in their cyclability as demonstrated in our previous work.[18] Moreover, the difference in the cracking pattern analysed for both electrodes indicates that the maturation process strongly modifies the mechanical properties of the binder phase in the composite electrode, allowing thus its network to better accommodate the volume variations. In other words, for the standard electrode, the binder acts as a "cement", and as a "plastic glue" for the matured electrode.

4. Experimental section

4.1. Materials

The active material was Si powder (99.999%, 20 mesh, Materion) ball-milled under argon atmosphere for 20 h using a SPEX 8000 mixer with a ball-to-powder mass ratio of 5:1. The Si powder (4.5 g) was introduced along with 3 stainless-steel balls (one of 14.3 mm diam. and two of 11.1 mm diam., total weight of 22.3 g) into a stainless-steel vial (55 mL). The fraction of amorphous Si in the milled powder was estimated at 63% from Raman analysis.[30] The obtained Si powder consists of micrometric agglomerates with a median size ~6 µm (determined by laser scattering method using a Malvern Mastersizer 2000) made of sub-micrometric particles more or less welded together. After the slurry mixing step (see below), the Si agglomerates are broken and the median size is reduced to 2.5 µm (**Figure S8,** Supporting Information). Graphene nanoplatelets (GnP) (M grade from XGSciences, average diameter = 15 µm, average thickness = 6-8 nm, surface area = 120-150 $m^2\ g^{-1}$ according to the supplier's data) was used as conductive additive. Carboxymethyl cellulose (CMC) (DS = 0.7, Mw = 90 000 g mol^{-1}, Sigma-Aldrich) was used as binder. Citric acid (99.5+%, Alfa Aesar) and KOH salts (85+%, Alfa Aesar) were used to prepare a pH3 buffer solution (0.17 M citric acid + 0.07 M KOH) as slurry medium.

4.2. Electrode preparation and cell assembly

A slurry was prepared by mixing 200 mg of powder (80 $\%^{wt}$ Si, 8 $\%^{wt}$ CMC and 12 $\%^{wt}$ GnP) in 0.5 mL of pH 3 buffer solution. Mixing was performed using a magnetic stirrer at 500 rpm for 1 h in presence of 3 silicon nitride balls (9.5 mm diam.). Flat copper current collectors were prepared by surface polishing of copper discs (3 mm diam., 1 mm thick). This step is mandatory to have a perfectly planar surface of copper and to resolve more clearly the current collector/electrode interface imaged by XRCT. The copper discs were coated with the slurry in order to reach an active mass loading of ~5.5 mg $_{Si}$ cm^{-2}. The electrodes were not calendered. After the coating step, the electrodes were dried at room temperature in air for 12

h. The labelled "standard electrode" was then dried at 100°C under vacuum. Before this final drying step, the labelled "matured electrode" was stored 2 days at room temperature in an environmental chamber at ~80% relative humidity (RH). The maturation conditions have been previously optimized as described elsewhere.[18] Note that the maturation accentuates the surface oxidation of the Si powder but this one has no significant impact on the electrode performance.[18]

The electrodes were mounted in a two-electrode Swagelok® cell compatible to the XRCT measurements. A schematic view of the electrochemical cell is presented in **Figure S1a** (Supporting Information). The cell housing was made of perfluoroalkoxy alkane (PFA) polymer with a wall thickness reduced to 2.5 mm near the electrode to ensure a lower X-ray attenuation and better image quality. The Si-based electrode was placed towards a lithium metal electrode (1 mm thick) deposited on a copper current collector, acting as a counter and reference electrode. The electrodes were separated with a borosilicate glass-fiber (Whatman GF/D) membrane soaked with an electrolytic solution of 1 M $LiPF_6$ in ethylene carbonate (EC) and dimethyl carbonate (DMC) (1:1) with 10 wt. % fluoroethylene carbonate (FEC). The good contact between the different components of the cell was ensured by a spring placed on the counter electrode side, which was slightly compressing the cell (load ~ 6 N).

4.3. *In situ* synchrotron XRCT measurements

In situ synchrotron XRCT analyses were performed at the Soleil synchrotron (Gif-sur-Yvette, France) for the standard electrode and at the ESRF (European Synchrotron in Grenoble, France) for the matured electrode. The electrochemical cell was placed perpendicularly to the propagation path of the X-ray beam. The Si electrodes were cycled at room temperature in galvanostatic mode at full capacity between 1 V and 5 mV *vs.* Li/Li^+ at a current density of 180 mA g^{-1} of Si (C/20) for the standard electrode and 600 mA g^{-1} of Si (C/6) for the matured electrode both in discharge (lithiation) and charge (delithiation) using a

OrigaFlex OGF500 potentiostat/galvanostat. A higher C rate was applied for the matured electrode due to a limited amount of beam time allocated for this experiment. The cell was left at the open circuit potential during the XRCT acquisition periods performed at regular intervals (typically, every hour).

For the XRCT experiments on the standard electrode performed at the Psiché beam-line of the Soleil facility, a beam monochromatized to 25±1 keV and a flux of 10^{13} ph s^{-1} were used. 1500 2D projections were recorded along a 180° cell rotation with 45 ms of exposure per projection on a CCD camera detector for a total acquisition time of ~1 min per scan. 3D tomographic volumes of 1333×1333×210 μm^3 with an isotropic voxel size of 650 nm were reconstructed in 32 bit floating-point representation from 2D projections using the PyHST2 software.[41] A volume of 190×190×210 μm^3 was extracted from the total acquired volume, in order to compare identical volumes for both standard and matured electrodes. The greyscale value in the final reconstructed volume represents the attenuation coefficient, so more attenuating (usually denser) regions appear brighter. The Fiji software was used for the image processing and analyses of the reconstructed volumes.[42] Image greyscale alignment was performed by taking the grey level of the separator as a reference.

XRCT acquisitions on the matured electrode were recorded at the nano-analysis end-station ID16B of the ESRF using holotomography.[43,44] Phase contrast imaging was acquired using a conic and monochromatic beam with an energy of 17.5 keV and a flux of 10^{12} ph s^{-1}. Four tomographies were acquired for four different distances between the detector and the sample along the beam propagation way. A set of 1499 projections were recorded on a PCO edge camera (2560×2160 pixels) along a 360° rotation with an exposure time of 150 ms per step. The pixels of the detector were binned (1280×1080 pixels) in order to have four times the flux per pixel and thus reducing the total acquisition time down to ~24 min per scan. A reconstructed volume of 256×256×210 μm^3 with an isotropic voxel size of 200 nm was obtained following a two-steps procedure: *(i)* phase retrieval calculation using an in-house

developed octave script based on a Paganin-like approach using a delta/beta~25 and *(ii)* filtered back-projection reconstruction using PyHST2 software.[41] Final volumes of $190\times190\times210$ μm^3 (after reforming) in a 32 bit floating point were obtained.

Details on the image segmentation procedure and on the quantitative analyse methods can be found in Supporting Information.

Supporting Information
Supporting Information is available from the Wiley Online Library or from the author.

Acknowledgements
The authors thank the Natural Sciences and Engineering Research Council (NSERC) of Canada (Grant No. RGPIN-2016-04524) for supporting this work. We thank also the Soleil synchrotron's reviewing committee for the shifts allocation. A particular thank to J. Villanova and J.P. Suuronen also for the time generously allocated for the measurements on the ID16B end-station at the ESRF. Finally a special thought for the precious help of Q. Lemarié, G. Meyruey, J. Adrien during the *in-situ* XRCT measurements.

Received: ((will be filled in by the editorial staff))
Revised: ((will be filled in by the editorial staff))
Published online: ((will be filled in by the editorial staff))

References

[1] M.N. Obrovac, V.L. Chevrier, *Chem. Rev*. **2014**, *114*, 11444.

[2] S. Goriparti, E. Miele, F. De Angelis, E. Di Fabrizio, R. Proietti Zaccaria, C. Capiglia, *J. Power Sources* **2014**, *257*, 421.

[3] Y. Jin, B. Zhu, Z. Lu, N, Liu, J. Zhu., *Adv. Energy Mater*. **2017**, *7*, 1700715.

[4] X. Zuoa, J. Zhua, P. Müller-Buschbaumb, Y-J. Chenga, *Nano Energy* **2017**, *31*, 113.

[5] X. H. Liu, L. Zhong, S. Huang, S. X. Mao, T. Zhu, J. Y. Huang, *ACS Nano* **2012**, *6*, 1522.

[6] M. Gauthier, D. Mazouzi, D. Reyter, B. Lestriez, P. Moreau, D. Guyomard, L. Roue, *Energy Environ. Sci*. **2013**, *6*, 2145.

[7] M.N. Obrovac, *Curr. Opin. Electrochem.* **2018,** *9*, 8.

[8] H. Shobukawa, J.Alvarado, Y. Yang, Y.S Meng. *J. Power Sources* **2017**, *359*, 173.

[9] E.M. Erickson, E. Markevich, G. Salitra, D. Sharon, D. Hirshberg, E. de la Llave, I, Shterenberg, A. Rozenman, A. Frimer, D. Aurbach. *J. Electrochem. Soc.* **2015**, *162*, A2424.

[10] A. Etiemble, A. Tranchot, T. Douillard, H. Idrissi, E. Maire, L. Roué, *J. Electrochem. Soc*. **2016**, *163*, A1550.

[11] D. Mazouzi, Z. Karkar, C. Reale Hernandez, P. Jimenez Manero, D. Guyomard, L. Roué, B. Lestriez. *J. Power Sources* **2015**, *280*, 533.

[12] J. Li, R.B. Lewis, J.R. Dahn, *Electrochem. Solid State Lett*. **2007**, *10*, A17.

[13] N.S. Hochgatterer, M.R. Schweiger, S. Koller, P.R. Raimann, T. Wöhrle, C. Wurm, M. Winter, *Electrochem. Solid State Lett.* **2008**, *11*, A76.

[14] D. Mazouzi, B. Lestriez, L. Roué, D. Guyomard, *Electrochem. Solid-State Lett.* **2009**, *12*, A215.

[15] J.T. Li, Z.Y. Wu, Y.Q. Lu, Y. Zhou, Q.S. Huang, L. Huang, S.G. Sun, *Adv. Energy Mater*. **2017**, *7*, 1701185.

[16] H. Chen, M. Ling, L. Hencz, H.Y. Ling, G. Li, Z. Lin, G. Liu, S. Zang, *Chem. Rev.* **2018**, *118*, 8936.

[17] Z. Karkar, D. Guyomard, L. Roué. B. Lestriez. *Electrochim. Acta* **2017**, *258*, 453.

[18] C.R. Hernandez, A. Etiemble, T. Douillard, D. Mazouzi, Z. Karkar, E. Maire, D. Guyomard, B. Lestriez, L. Roué, *Adv. Energy Mat.* **2017**, *8*, 1701787.

[19] Z. Karkar, T. Jaouhari, A. Tranchot, D. Mazouzi, D. Guyomard, B. Lestriez, L. Roué. *J Power Sources* **2017**, *371*, 136.

[20] F. Tariq, V. Yufit, D. S. Eastwood, Y. Merla, M. Biton, B. Wu, Z. Chen, K. Freedman, G. Ofeer, E. Peled, P. D. Lee, D. Golodnitsky, N. Brandon, *ECS Electrochem. Lett*. **2014**, *3*, A76.

[21] J. Gonzalez, K. Sun, M. Huang, J. Lambros, S. Dillon, I. Chasiotis, *J. Power Sources* **2014**, *269*, 334.

[22] F. Sun, H. Markötter, I. Manke, A. Hilger, N. Karddjilov, J. Banhart, *ACS Appl. Mater. Interf.* **2016**, *8*, 7156.

[23] F. Sun, H. Markötter, K. Dong, I. Manke, A. Hilger, N. Karddjilov, J. Banhart, *J. Power Sources* **2016**, *321*, 174.

[24] J.M. Paz-Garcia, O.O. Taiwo, E. Tudisco, D.P. Finegan, P.R. Shearing, D.J.L Brett, S.A. Hall, *J. Power Sources* **2016**, *320*, 196.

[25] O. O. Taiwo, J.M. Paz-García, S. A. Hall, T. M.M. Heenan, D. P. Finegan, R. Mokso, P. Villanueva-Perez, A. Patera, D.J.L. Brett, P.R. Shearing, *J. Power Sources* **2017**, *342*, 904.

[26] L. Zielke, F. Sun, H. Markötter, A. Hilger, R. Moroni, R. Zengerle, S. Thiele, J. Banhart, I. Manke, *Chem. Electro. Chem*. **2016**, *3*, 1170.

[27] P. Pietsch, D. Westhoff, J.Feinauer, J. Eller, F. Marone, M. Stampanoni, V. Schmidt, V. Wood, *Nat. Comm*. **2016**, *7*, 12909.

[28] V. Vanpeene, A. Etiemble, A. Bonnin, E. Maire, L. Roué, *J. Power Sources* **2017**, *350*, 18.

[29] P. Pietsch, M. Hess, W. Ludwig, J. Eller, V. Wood, *Sci. Rep*. **2016**, *6*, 27994.

[30] V. Vanpeene, A. King, E. Maire, L. Roué, *Nano Energy* **2019**, *56*,799.

[31] C. Zhao, T. Wada, V. De Andrade, D. Gürsoy, H. Kato, Y.K. Chen-Wiegart, *Nano Energy* **2018**, *52*, 381.

[32] F. Sun., L. Zielke, H. Markötter, A. Hilger, D. Zhou, R. Moroni, R. Zengerle, S. Thiele, J. Banhart, I. Manke, *ACS Nano* **2016**, *10*, 7990.

[33] F. R. Brushett, L. Trahey, X. Xiao, J. T. Vaughey, *ACS Appl. Mater. Interf.* **2014,** *6*, 4524.

[34] D. Mazouzi, D Reyter, M. Gauthier, P. Moreau, D. Guyomard, L. Roué, B. Lestriez, *Adv. Energy Mater*. **2014**, *4*, 1301718

[35] M. D. Thouless, *J. Vac. Sci. Technol. A* **1991**, *9*, 2510.

[36] J.R. Rice, *J. Appl. Mech*. **1988**, 55, 98.

[37] C. Creton, in *Adhesive Joints: Formation, Characteristics and Testing*, Vol. 2 (Eds: K.L. Mittal), VSP, Utrecht, Netehrlands **2002**, pp. 49-60.

[38] J.F. Barrett, N. Keat, *Radiographics* **2004**, *24*, 1679.

[39] M.T. McDowell, S. W. Lee, J. T. Harris, B. A. Korgel, C. Wang, W. D. Nix, Y. Cui. *Nano Lett.* **2013**, *13*, 758.

[40] X. Wang, F. Fan, J. Wang, H. Wang, S. Tao, A. Yang, Y. Liu, H. B. Chew, S.X. Mao, T. Zhu, S. Xia. *Nat. Commun.* **2015**, *6*, 8417.

[41] A. Mirone, E. Brun, E. Gouillart, P. Tafforeau, J. Kieffer, Nucl. Instrum. *Methods Phys. Res. B* **2014**, 324, 41.

[42] J. Schindelin, I. Arganda-Carreras, E. Frise, V. Kaynig, M. Longair, T. Pietzsch, S. Preibisch, C. Rueden, S. Saalfeld, B. Schmid, J.Y. Tinevez, D. J. White, V. Hartenstein, K. Eliceiri, P. Tomancak, A. Cardona, *Nat. Methods* **2012**, *9*, 676.

[43] G. Martinez-Criado, J. Villanova, R. Tucoulou, D. Salomon, J.-P. Suuronen, S. Labouré, C. Guilloud, V. Valls, R. Barrett, E. Gagliardini, Y. Dabin, R. Baker, S. Bohic, C. Cohen, J. Morse, *J. Synch. Rad.* **2016**, *23*, 344.

[44] P. Cloetens, W. Ludwig, J. Baruchel, *Appl. Phys. Lett*. **1999**, *75*, 2912.

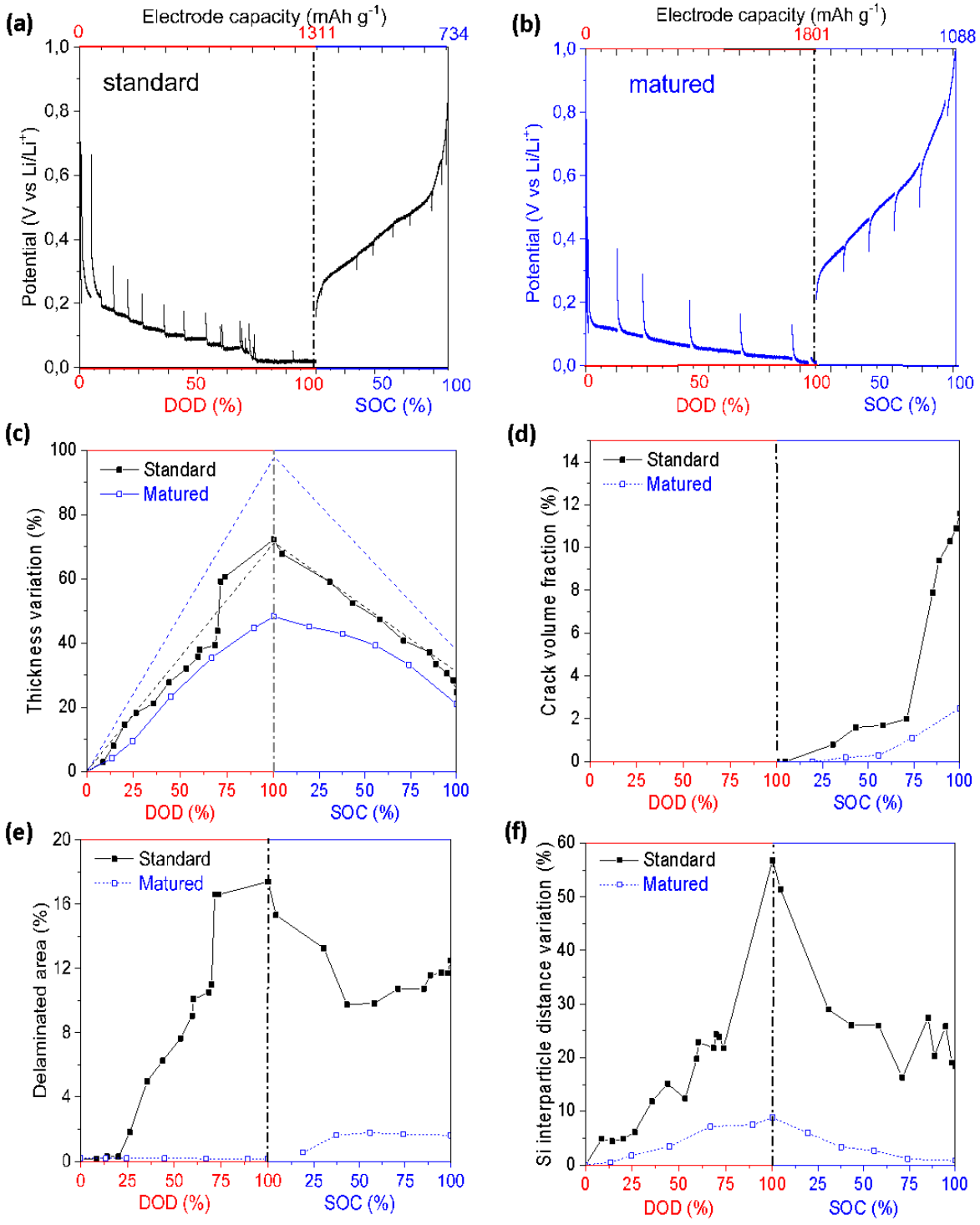

Figure 1. Evolution during the first cycle of the potential for the (a) standard and (b) matured electrode, (c) thickness change *(the theoretical variation in thickness assuming no change in percent porosity is shown for comparison (dotted lines))*, (d) crack volume fraction, (e) delaminated area and (f) Si interparticle distance variation for the standard (black curves) and matured (blue curves) electrodes. The analyzed volume is 190 × 190 × 210 μm^3 for both electrodes.

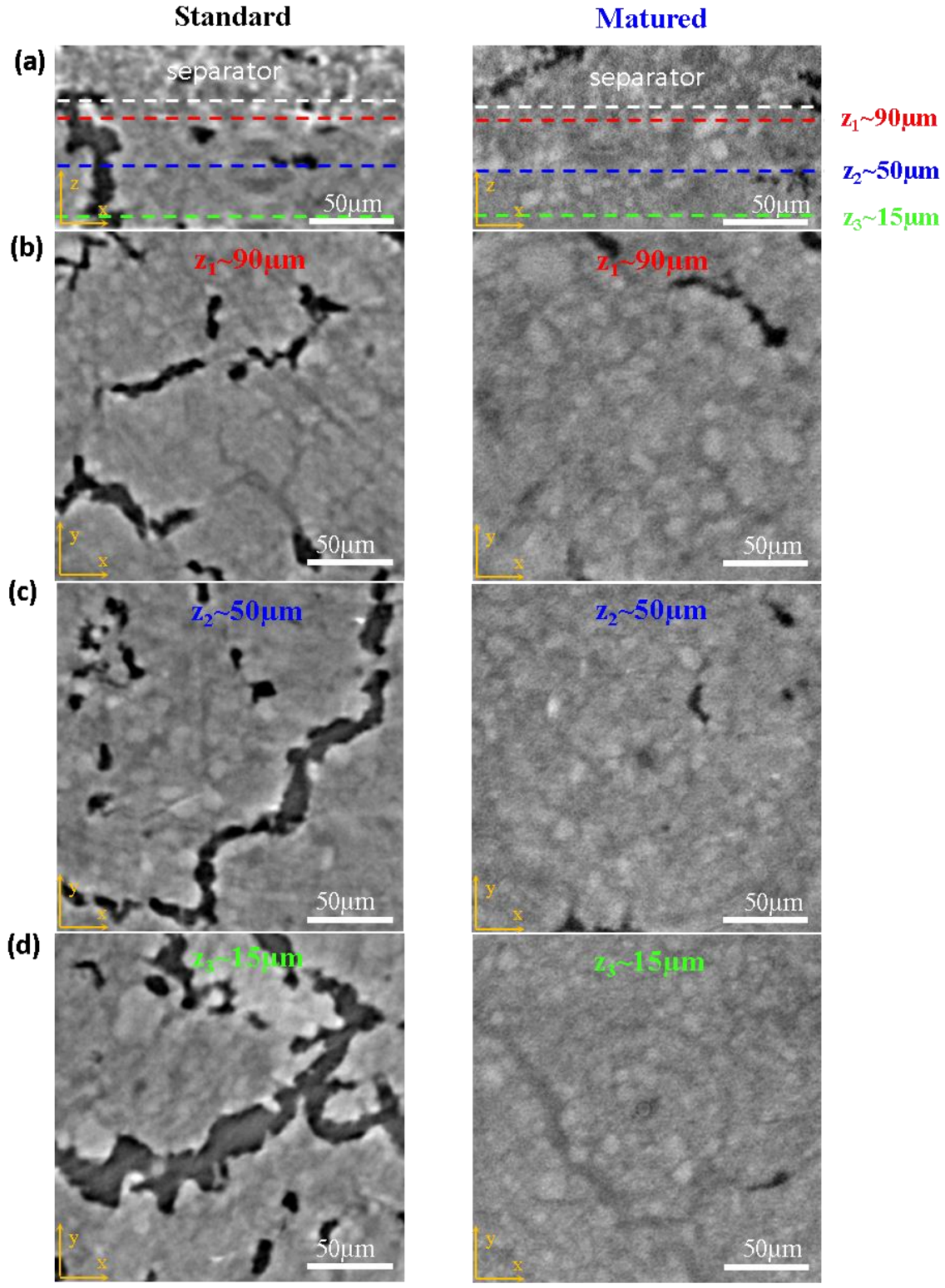

Figure 2. XRCT slice images in the (a) transversal *x*-*z* plan and (b-d) lateral *x*-*y* plans at different *z* positions, namely (b) near the separator (z_1~90 µm), (c) in the middle zone (z_2~50

μm) and (d) near the current collector (z_3~15 μm) of the standard (on left) and matured (on right) electrodes at the end of the 1st cycle. The white dashed line on the transversal images sets the interface between the top of the electrode and the bottom of the separator.

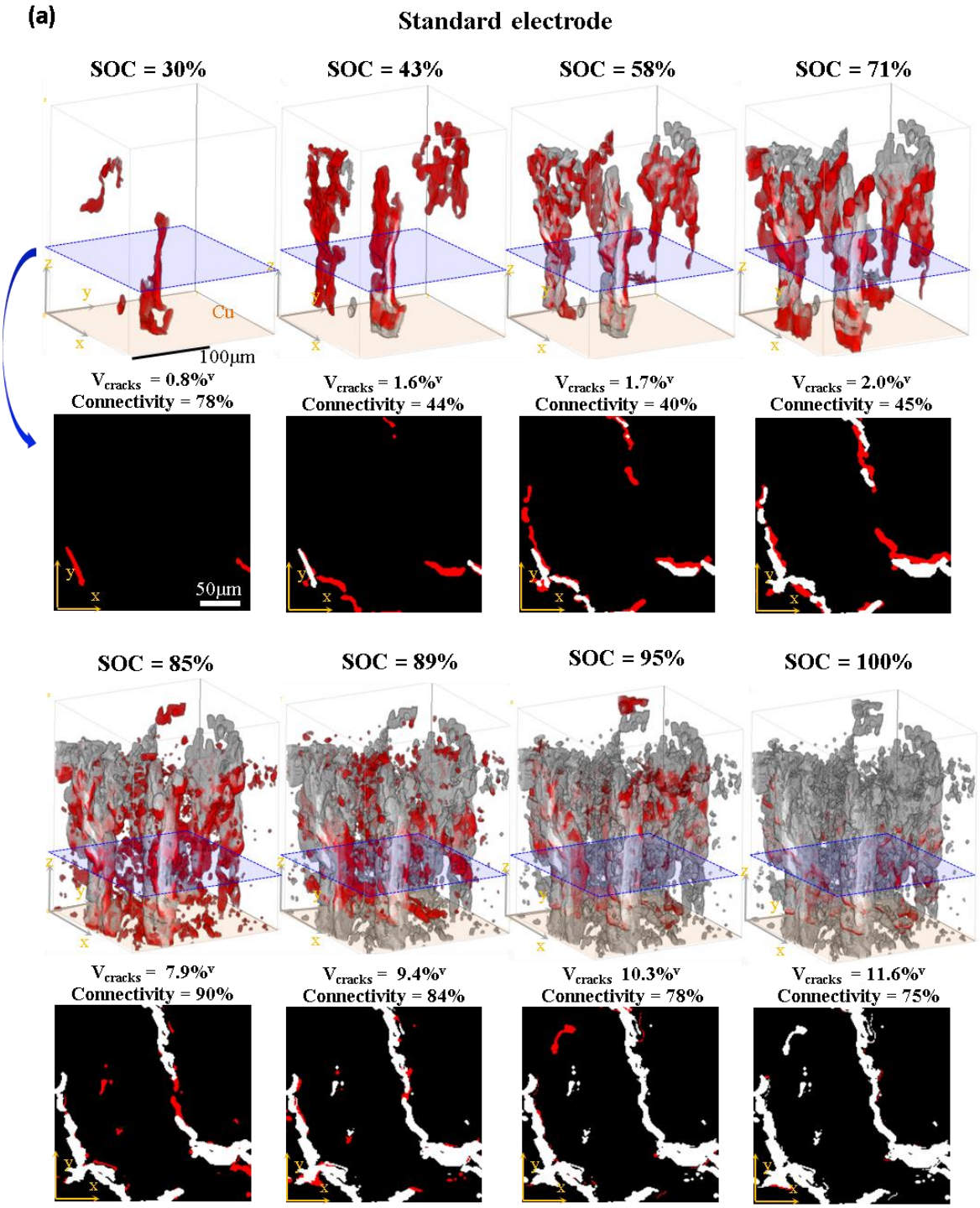

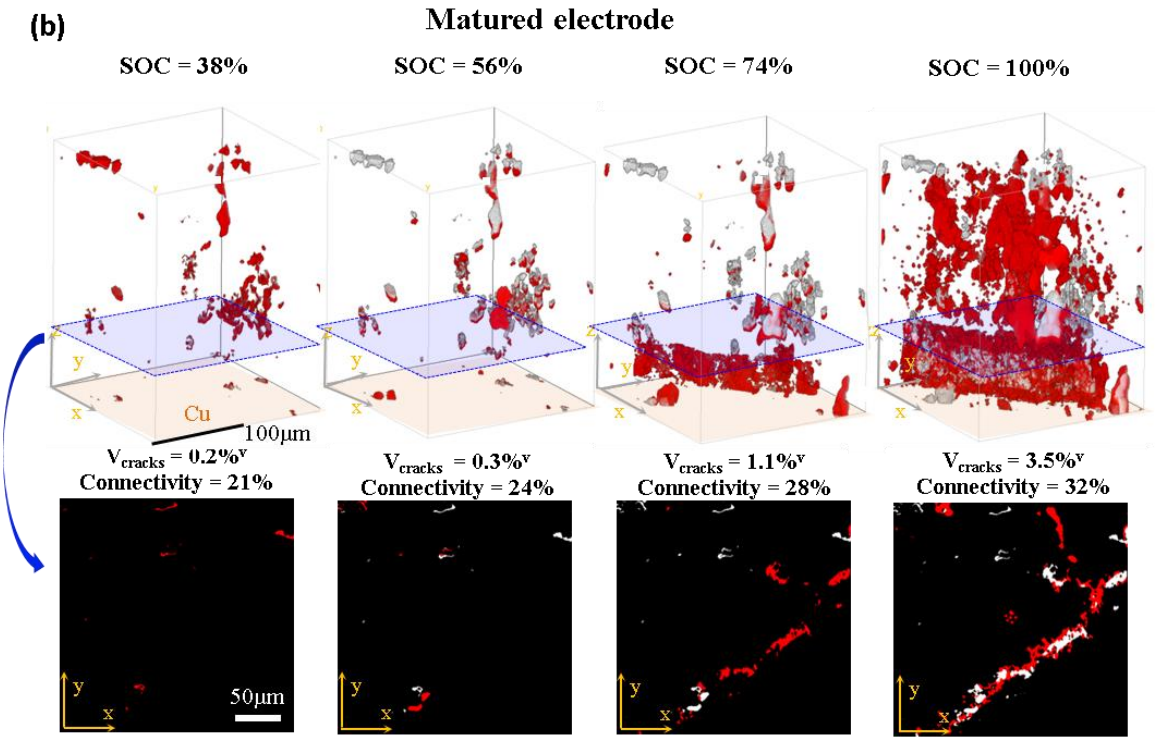

Figure 3. 3D rendering of the crack formation with increasing state-of-charge (SOC) for the (a) standard and (b) matured electrodes. The crack formation is also shown in 2D lateral (x,y) views corresponding to the dashed blue area displayed in the 3D views. The cracks formed at each charge step are highlighted in red and those formed during the previous steps are in grey in 3D views or white in 2D views.

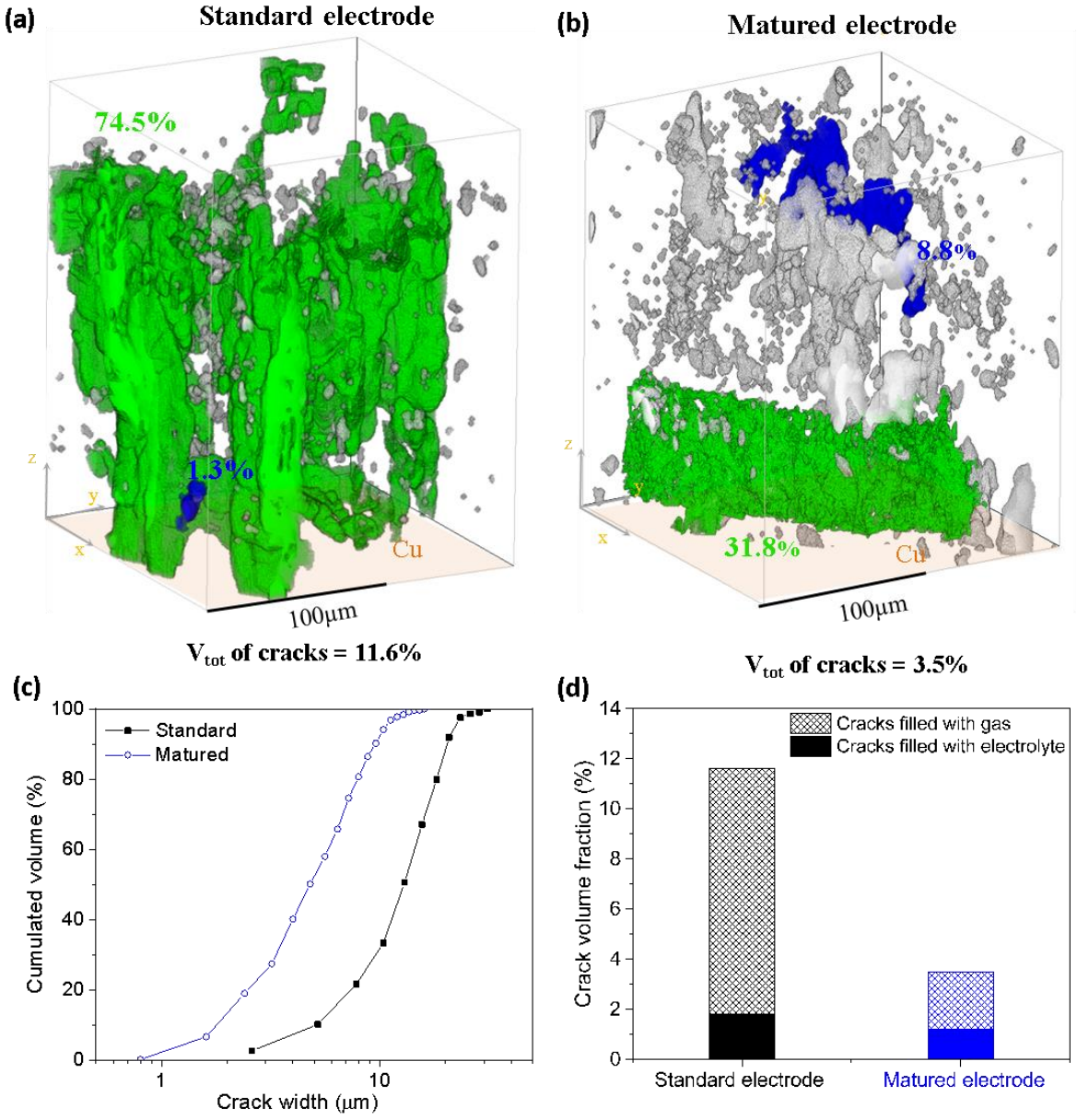

Figure 4. 3D rendering of the cracks at the end of the 1st cycle for the (a) standard and (b) matured electrodes. The green islet is the largest intra-connected volume of cracks and the blue is the second largest one; (c) distribution of the crack width and (d) histograms of proportion of cracks filled with gas or electrolyte for the standard and matured electrodes at the end of 1st cycle.

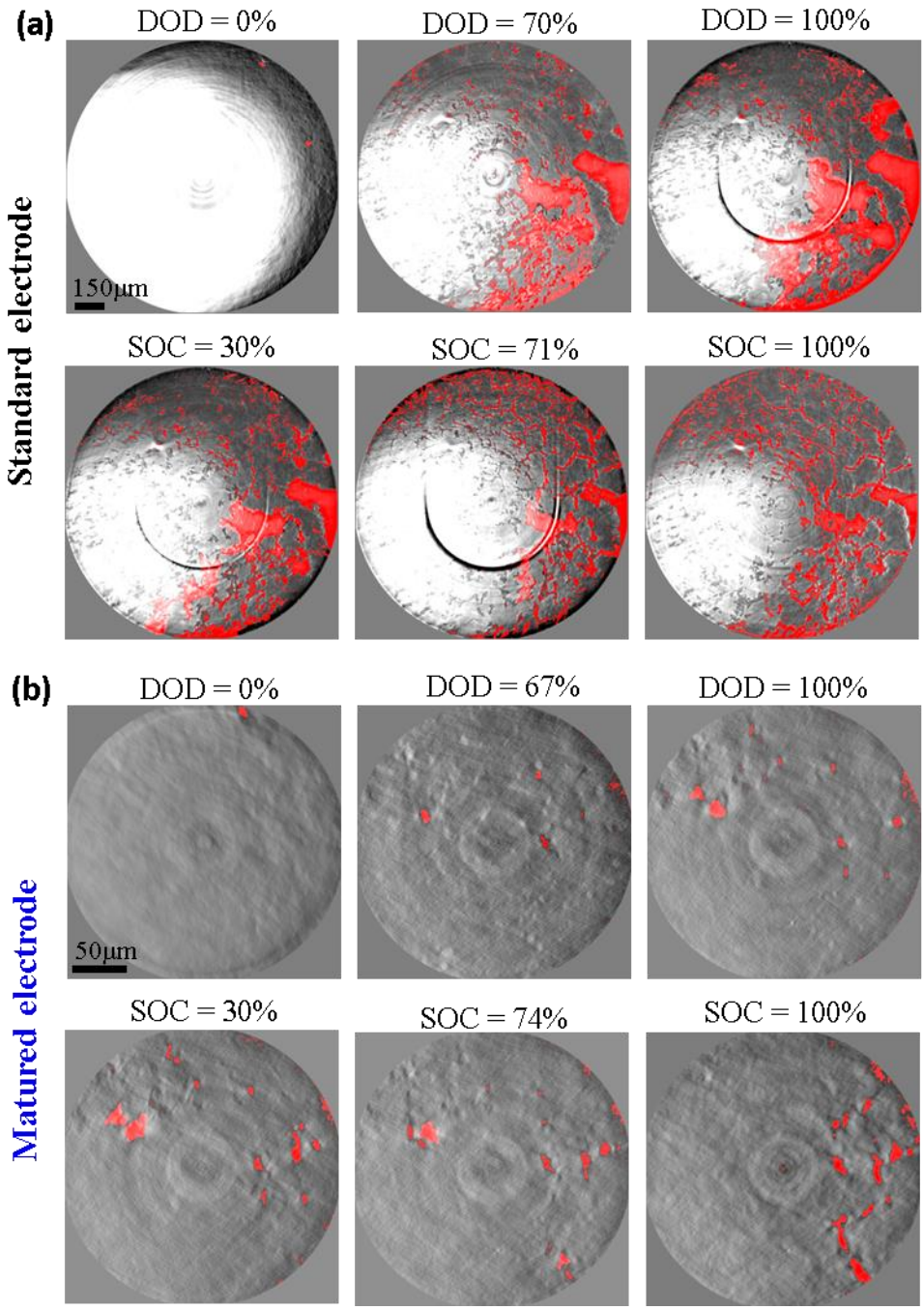

Figure 5. XRCT lateral images of the Cu/electrode interface showing the formation of delaminated zones (highlighted in red) during the 1st discharge/charge for (a) the standard and (b) matured electrodes.

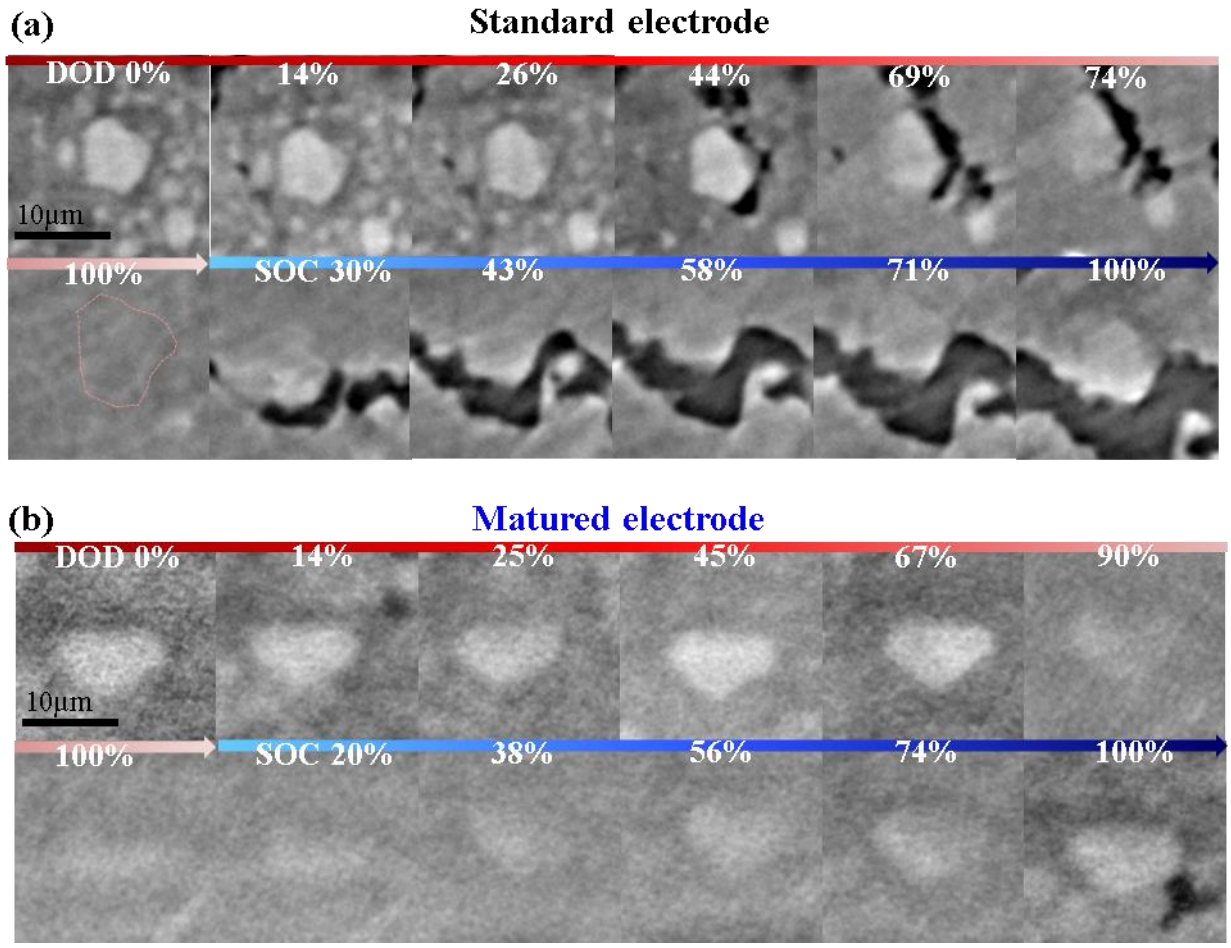

Figure 6. Evolution during the 1st cycle of XRCT lateral images focused on a large Si particle for the (c) standard and (d) matured electrodes.

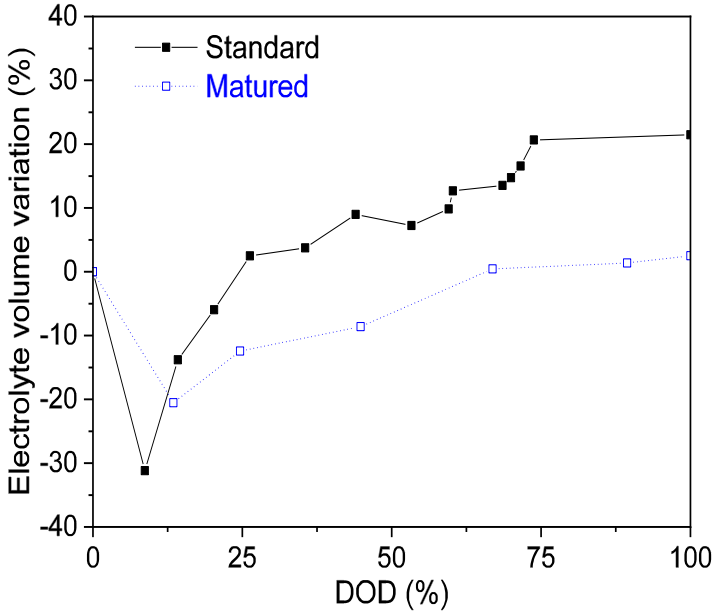

Figure 7. Relative variation of the electrolyte volume for the standard (black curve) and matured (blue curve) electrodes during the 1st discharge. The analyzed volume is 190 × 190 × 210 μm^3 for both electrodes.

Table 1. Main morphological characteristics (volume fraction ϕ_v, intra-connectivity c, median diameter d_{50}) of the different domains identified from XRCT analyses for the standard and matured electrodes at the pristine state, after the 1st discharge and after the 1st charge

		Pristine			1st discharge			1st charge		
		ϕ_v (%)	c (%)	d_{50} (µm)	ϕ_v (%)	c (%)	d_{50} (µm)	ϕ_v (%)	c (%)	d_{50} (µm)
Standard electrode	Solid phase	60.7	99.9	-	77.5	99.9	-	65.5	98.2	-
	Gas-filled pores	2.1	20.4	6.6	2.7	11.6	9.5	10.1*	42.9*	11.2*
	Electrolyte-filled pores	37.2	98.1	5.2	19.8	93.1	2.6	24.4*	95.3*	2.8*
	Total pores	39.3	95.4	5.4	22.5	93.3	7.7	34.5*	92.7*	10.3*
	Cracks	-	-	-	-	-	-	11.6	74.5	13.1
	Delaminated area**	0.1	-	-	17.4	-	-	12.5	-	-
Matured electrode	Solid phase	61.6	99.5	-	81.3	99.9	-	66.7	99.9	-
	Gas-filled pores	3.1	23.4	3.8	0.7	46.5	4.6	2.9*	12.7*	6.4*
	Electrolyte-filled pores	35.3	97.6	1.9	18.0	91.6	2.0	30.4*	98.1*	2.3*
	Total pores	38.4	97.9	2.6	18.7	91.8	2.9	33.3*	98.4*	3.2*
	Cracks	-	-	-	-	-	-	3.5	31.8	4.8
	Delaminated area**	0.2	-	-	0.2	-	-	1.6	-	-

* including cracks ** expressed in area fraction ϕ_s (%)

Supporting Information

Dynamics of the morphological degradation of Si-based anodes for Li-ion batteries characterized by *in-situ* synchrotron X-ray tomography

Victor Vanpeene, Julie Villanova, Andrew King, Bernard Lestriez, Eric Maire and Lionel Roué**

Electrode	Cycling conditions	Si particle diam. (µm)	Imaged volume / Electrode thickness	Voxel size (µm)	In situ /ex situ	Qualitative observations	Quantitative observations	Ref
C-coated Si/CB/CMC (70/20/10%^{m}) on Cu tip	I = 2.4 mA/cm^2 (~C/4) for 1 h in 1M $LiPF_6$ EC:DEC (1:1) + 2% VC	0.03	8 mm^3 ~300 µm	9.3	In situ	Electrode expansion and delamination	Delamination width and height	**[20]**
Si/CB/PVdF (75/15/10%^{m}) on Ti foil	I~60 mA/g Si discharge (~C/60) and ~15 mA/g Si charge (~C/240) for 1 cycle in 1M LiPF6 EC:DMC (1:1)	125-180	200 µm	5.76	In situ	- presence of inactive Si particles at the pristine state - desactivation of some Si particles during the charge	- Si particle volume expansion - Attenuation coefficient evolution of Si particles upon cycling	**[23]**
Si/CMC+CB (22/78%^{m}) on Cu rod	I= C/80 – C/160 for the 1st discharge in 1M LiClO4 EC:DMC (1:1)	<105	1810×1810×1860 µm^3 ~2000 µm	1.89	In situ	- Si particle expansion and cracking - Core-shell lithiation - faster lithiation of the smaller Si particles	- Evolution of the attenuation coefficient of the Si particles as a function of lithiation - volume expansion of Si particles as a function of their distance from the separator and their lithiation level	**[21]**
Si/CB/PVdF (80/10/10%^{m}) on stainless steel pin	I= C/300 for the 1st discharge in 1M LiPF6, EC:EMC (3:7)	<50	3400×3400×800 µm^3 ~400 µm	1.7	In situ	- electrode volume expansion - separator rupture - Si particle volume expansion - Core-shell lithiation	- Volume expansion and strain measured by digital volume correlation (DVC)	**[24]**
Si/CB/PVdF (50/25/25%^{m}) on Cu foil	E= 10mV/Li for 15h in 1M LiPF6 EC:DEC (1:1)	1- 20	1590×1590×930 µm^3 ~200 µm	1.55	In situ	- electrode volume expansion - Formation of $Li_{15}Si_4$ (in-situ XRD) - inhomogeneous lithiation	SOC map based on the evaluation of the local attenuation coefficient of the electrode	**[29]**
Si/CB/PVdF (70/10/20%^{m}) on Cu	I= ~C/25-C/150 for ? cycles in 1,2M LiPF6, EC:EMC (3:7)	<44	2200×2200×110 µm^3 ~60 µm	1.1	Ex situ	- post-mortem observation - Si pulverization -SEI formation	- electrode volume expansion - electrode porosity evolution	**[33]**

Si/CB/PVdF (80/10/10%^{m})	I=1.75 A/g Si (~C/2) for 1.5 cycles in 1M LiPF6 EC:DMC (1:1)	5-30	-	0.876	In situ	- formation of gas bubbles and channels	- gas volume fraction - fraction of active Si particles	**[22]**
Si/CB/PVdF (30/60/10%^{m}) on stainless steel pin	I= C/70 for the 1st discharge in 1M LiPF6, EC:EMC (3:7)	<50	1600×1600×1400 µm^3 54 µm	0.65	In situ	- Si particle cracking - inhomogeneous lithiation	evolution of the attenuation coef., surface area and residual c-Si volume of Si particles	**[25]**
Si/GnP/CMC (80/12/8%^{m}) on C paper	I= C/9 for 1st and 10th cycles in 1M LiPF6 EC:DMC (1:1) + 10% FEC	~2.5	943×943×208 µm^3 ~100 µm	0.65	In situ	- electrode volume change and cracking - Si particle lithiation and delithiation - Gas formation - SEI formation	- dimensional change of the electrode - variation of the volume fraction of solid and pore phases - Porosity evolution	**[30]**
Si/CB/PVdF (70/20/10%^{m}) on stainless steel	I= C/30 for 1st discharge in 1M LiPF6 EC:EMC (1:1)	~7	1700×1700×200 µm^3 ~160 µm	0.438	In situ	- inhomogeneous Si particle cracking - inhomogeneity of lithiation	- Si particle size and surface area - volume fraction of fractures within Si particles - local Si particle size distribution - local cavity fraction distribution	**[26]**
Si/CB/CMC (80/12/8%^{m}) on Cu foil	I= C/6 or C/20 for 1 cycle in 1M LiPF6 EC:DMC (1:1) + 10% FEC	~2.5	190×190×210 µm^3 ~95 µm	0.65/0.2	In situ	- electrode cracking dynamic - electrode delamination dynamic - Si particle lithiation and delithiation	- dimensional change of the electrode - Crack volume fraction - delaminated area - Si inter-particle distance - volume fraction, intra-connectivity and median diameter of the solid, gas and electrolyte phases.	**This work**
Si/CB/CMC (80/12/8%^{m}) on C paper	I=C/9 for 1.5 cycles in 1M LiPF6 EC:DMC (1:1)	~0.2	293×293×137 µm^3 90µm	0.16	In situ	- electrode expansion /contraction - gas evolution - SEI formation - electrode cracking	- dimensional change of the electrode - evolution of the volume fraction, size and intraconnectivity of the solid, electrolyte and gas phases	**[28]**

Si/CB/PI (60/25/15%^{m}) on Cu	I=C/2 (1-10 cycles) and C (100-1500 cycles) Q=1000 or 2000mAh g^{-1} in 1M $LiPF_6$ FEC	~0.4	52×52×62 µm^3 ~2 µm	0.06	Ex situ	- electrode swelling - formation of pores - partial delamination - material density evolution - Si particle agglomeration	- electrode thickness evolution - attenuation coefficient evolution with cycling and as a function of the distance from the current collector	**[31]**

Table S1. Summary of the literature data on XRCT studies of Si-based anodes. They are classified along their spatial resolution. The reference numbers correspond to those labelled in the full paper.

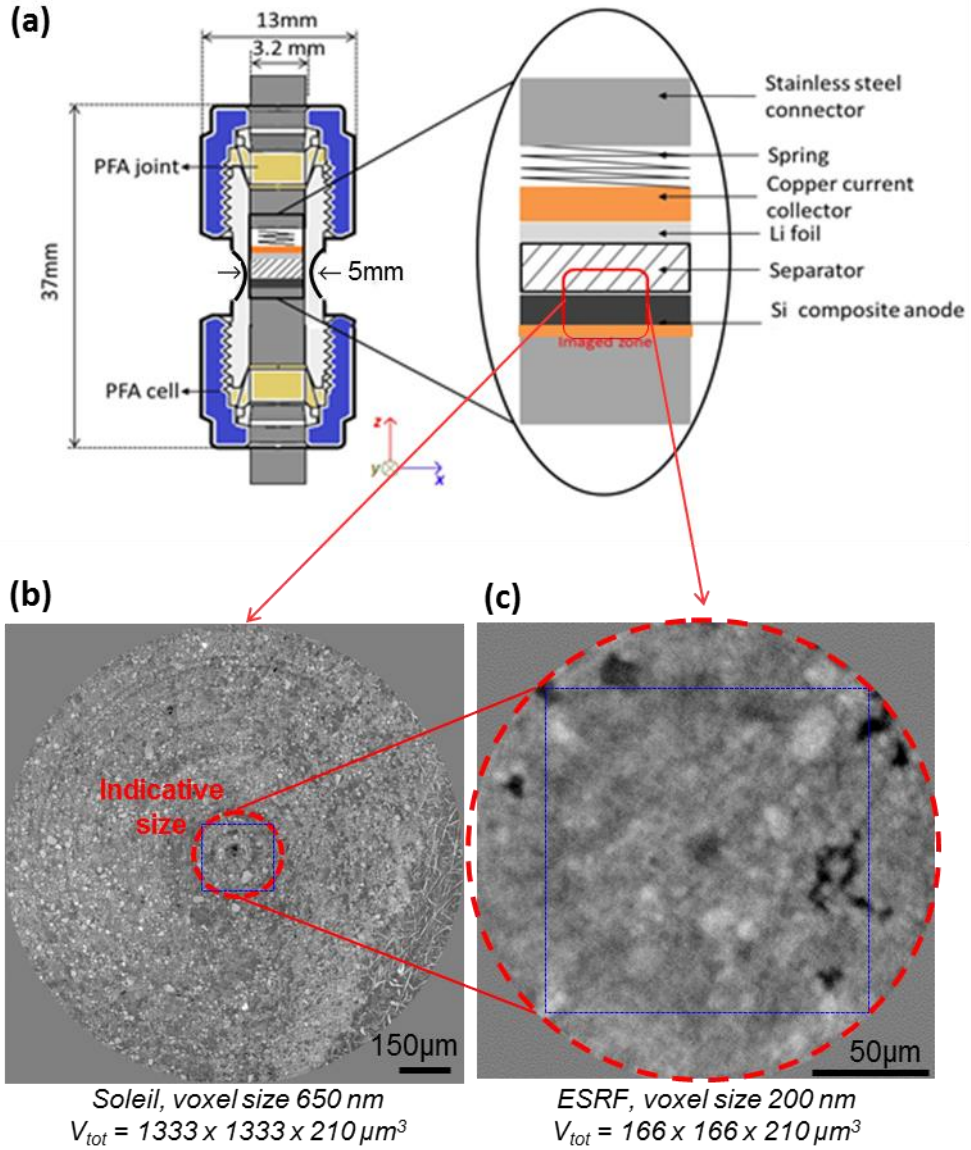

Figure S1. (a) Schematic representation of the electrochemical cell used for *in-situ* XRCT experiments. XRCT images in the lateral (x,y) plan of the (b) standard electrode and (c) matured electrode acquired at Soleil and ESRF synchrotron, respectively. The red circle is the indicative size of the ESRF imaged volume. The blue square is the indicative size of the compared volume (190 × 190 × 210 µm^3) for both electrodes.

Discussion on the representativeness of the studied volume

In order to compare identical volume size for the matured and standard electrode, a sub-volume of 190×190×210 µm^3 has been extracted from their respective total reconstructed volumes. The apparent heterogeneity of the electrode material questions the representativeness of this sub-volume versus the whole electrode volume. For that purpose, sub-domains of different sizes of $a \times a \times 210$ µm^3 with a ranging from 98 to 1333 µm were analysed. The mean volume fraction of solid phase and its standard deviation were determined for each sub-volume from ten measurements performed in different regions of the electrode. By taking under consideration the fact that the electrode structure changes drastically during the 1st cycle, these analyses were performed at the pristine state (**Figure S2a**) and at the end of the 1st cycle (**Figure S2b**) on the standard electrode. The exact value is assumed to be the one measured for the total reconstructed volume of 1333 × 1333 × 210 µm^3. The green area corresponds to an error interval of ±10% from the exact value. It appears that the measured mean values are very close to the exact value whatever the analyzed domain size. However, the lower the domain size, the larger the standard deviation. As seen in **Figure S2b**, a similar tendency is observed for the cycled electrode but with larger standard deviation values. From these analyses, the morphological parameters extracted from a sub-volume of 190×190×210 µm^3 are assumed to be representative of the whole electrode volume.

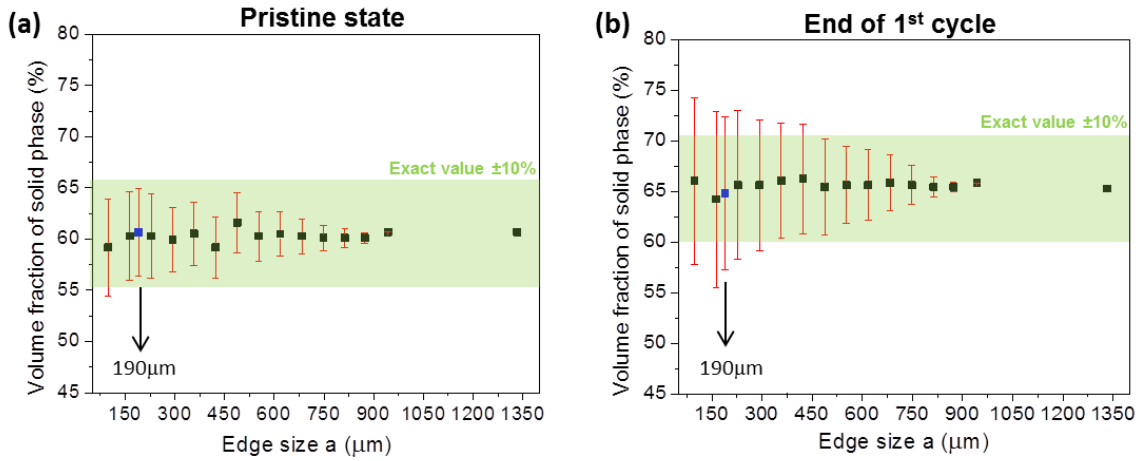

Figure S2. Evolution of the mean volume fraction of solid phase in the standard electrode (a) at the pristine state and (b) after the 1st cycle as a function of the analyzed domain size.

Details on the segmentation procedure

Separator.– The separator attenuates strongly the X-ray beam and has very well defined edges. It can thus be easily isolated by thresholding on the high value of the greyscale histogram. By selecting the high grey value, some of the brightest parts of the electrode are however selected as well, corresponding to the abrupt edges of the electrode. In order to eliminate them, a labeling step is additionally used. This procedure classifies the different interconnected objects in the volume. The biggest inter-connected part of the volume corresponds to the filament-like structure of the separator.

Gas phase. – Then the gas phase (*i.e.* electrolyte-free pores), which is the lowest attenuating part of the electrode, is isolated by thresholding on the low grey values of the images. The thresholding level is placed qualitatively regarding the greyscale histogram and the features in the image. Only the outlines are obtained and an additional step was added for filling the "holes" using a dedicated plugin on the Fiji software. The resulting segmented volume of the gas phase is represented in grey in Figures **S3c-d**.

Electrolyte and solid phases.– The mean attenuation coefficients values of the electrolyte and solid phases are close. Thanks to the phase-contrast based images, which enhance the contrast at the material interfaces, the separation is achieved by thresholding on the low grey scale value. The thresholding level is placed qualitatively regarding the greyscale histogram and the features in the image. Furthermore, the density of the solid phase changes with cycling due to the Si lithiation/delithiation, thus its mean attenuation coefficient decreases while lithiated and increases otherwise. Therefore the thresholding level was adjusted at each step of cycling by considering the grey level of the separator as a reference. The isolated electrolyte and solid phase are represented in red in **Figure S3a-b** and in cyan in **Figure S3c-d**, respectively.

Si particles. – Within the solid phase, the C-rich components (i.e. CMC, GnP and CA) cannot be differentiated as they have nearly the same mean attenuation coefficient. Regarding the Si phase, only the largest Si particles/clusters, *i.e.* having a size higher than the present XRCT spatial resolution of ~1.3 µm (for the standard electrode) or ~0.4 µm (for the matured electrode), can be isolated as shown in yellow in **Figure S3a-b**.

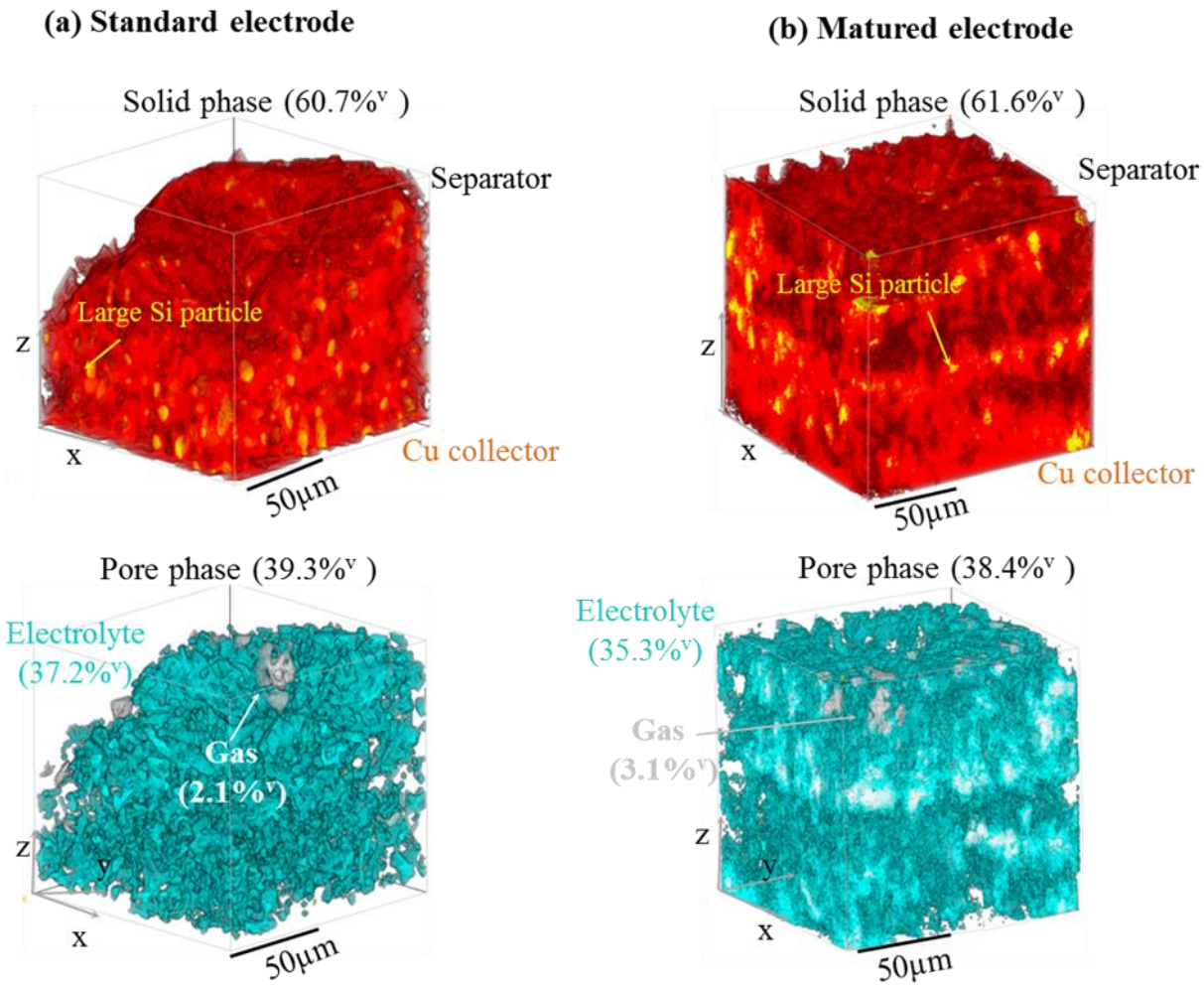

Figure S3. 3D views of the segmented solid phase (in red with large Si particles in yellow), electrolyte-filled pores (in cyan) and gas-filled pores (in grey/white) for the (a) standard and (b) matured electrodes at the pristine state.

Details on the quantitative analyses of the XRCT images

Dimensional change. The variation of the electrode thickness was determined from the displacement of the interface between the electrode and the separator. This interface was determined from lateral images, where the separator composed of interconnected borosilicate fibers appears clearly in bright on the greyscale images. As the electrode surface is not perfectly flat, the separator/electrode interface is set by considering the mean z position where the electrode is not predominantly present. The lateral dimensional changes were estimated by evaluating the variation of geometrical distances between specific features of the electrodes, *i.e.* by considering gas-filled pores and large Si particles. These measurements were repeated and averaged along the electrode thickness.

Volume fraction. The volume of an identified (segmented) phase, V_{phase}, was estimated using a marching cube algorithm **[1]**. It corresponds to the volume included in the isosurface of the identified phase. The electrode volume, $V_{electrode}$, is deduced by addition of the volumes of the different segmented phases. The volume fraction of a given phase is then calculated as the ratio $V_{phase} / V_{electrode}$.

Intra-connectivity. The intra-connectivity of an identified phase was estimated by using a "labelling" method allowing identifying the independent 3D objects of a volume. Each object, defined as a cluster of connected voxels, is labelled with a different grey value. The intra-connectivity of a phase is then calculated as the ratio of the volume of the largest cluster of the phase over the entire phase volume.

Size distribution. The size (diameter) of the pores and cracks was estimated thanks to a dedicated mathematical morphology operation. This process involves successive erosion and dilation steps of the image for structural elements of size *n*. The difference between each dilated and eroded image allows retrieving the amount of elements of size *2n* in the image. The structural element chosen here is a sphere.

Crack growth. The cracks formed in the electrode volume are newly formed elements with the greyscale value of the electrolyte phase or gas phase. The fraction of cracks formed at each acquisition step was estimated by subtracting the binary images of the porosity at the current step from that of the previous one. The operation is repeated for all acquisition steps by considering separately the electrolyte and gas filled porosities. Noise reduction by image erosion and manual corrections were added in order to avoid parasitic effects of the volume contraction. These corrections are crucial for the electrolyte-filled porosity, which is noisier than the gas-filled porosity. Then both crack images are summed. 3D rendering were obtained from an in-house developed plug-in implemented in the Fiji software **[2]**.

Delaminated surface area. The delaminated surface area was estimated from the porosity at the electrode/current collector interface. Since this porosity is less attenuating the beam, it appears darker and thus can be isolated by thresholding on the low greyscale value of the histogram at each acquisition step. Manual corrections were mandatory in order to avoid the parasitic effect of the star-burst artefacts present at the electrode/Cu interface.

Details on the calculation of the theoretical variation in thickness presented in Fig. 1c.

Assuming no change in the percent porosity (i.e. the pores expands by the same amount that the Si particles) and that the variation of the electrode thickness is equivalent to its volume variation (i.e. the electrode expands only in the out-of-plane direction) and that all the discharge capacity is associated with the formation of $SiLi_x$ (i.e. SEI formation is not considered), the theoretical variation in electrode thickness can calculated according to the following equation:

$$\Delta h_{el}(\%) = \emptyset_{m,Si} \times \frac{\rho_{theo}}{\rho_{Si}} \times \Delta V_{Si}(\%) \times Q_{Si} = 0.0541 \times Q_{Si}$$

where $\phi_{m,Si}$ is the Si mass fraction in the pristine electrode (0.732), ρ_{theo} is the true density of the pristine electrode (2.20 g cm^{-3}) **[3]**, ρ_{Si} is the true density of Si (2.33 g cm^{-3}), ΔV_{Si} is the intrinsic volume expansion of $SiLi_x$ (0.0782% per mAh/g Si since its expansion is 280% for x = 3.75 or 3579 mAh/g) **[4]** and Q_{Si} is the measured electrode capacity (mAh/g Si).

[1] WE Lorensen, HE Cline, *ACM SIGGRAPH Computer Graphics* **1987**, 21, 163.

[2] J. Schindelin, I. Arganda-Carreras, E. Frise, V. Kaynig, M. Longair, T. Pietzsch, S. Preibisch, C. Rueden, S. Saalfeld, B. Schmid, J.Y. Tinevez, D. J. White, V. Hartenstein, K. Eliceiri, P. Tomancak, A. Cardona, *Nat. Meth.* **2012**, 9, 676.

[3] Z. Karkar, T. Jaouhari, D. Mazouzi, D. Guyomard, B. Lestriez, L. Roué, *J. Power Sources* **2017**, 371, 136.

[4] M. N. Obrovac, L. J. Krause, J. *Electrochem. Soc*. **2007**, 154, A103.

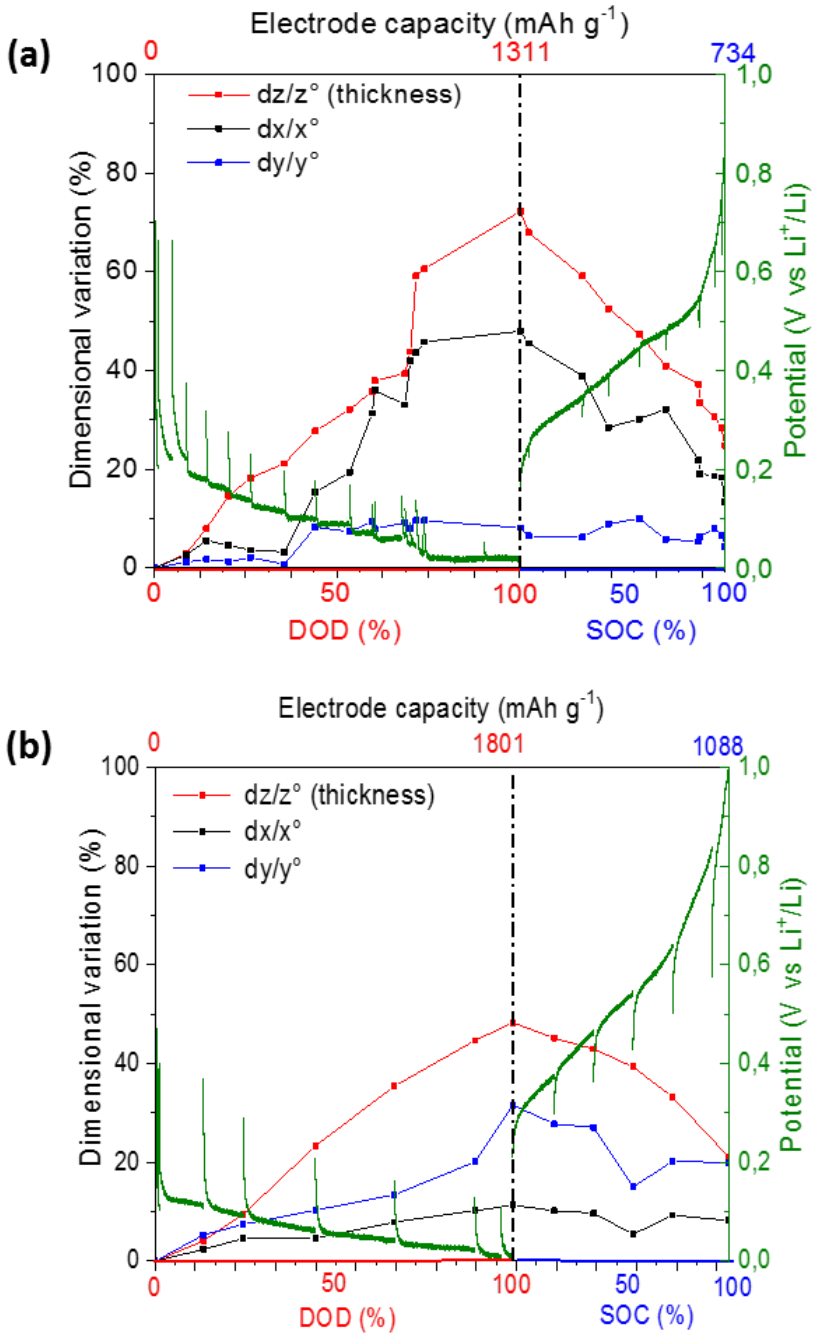

Figure S4. Relative variation of the lateral (*x, y*) and transversal (*z*) dimensions of the (a) standard electrode and (b) matured electrode during the 1st cycle.

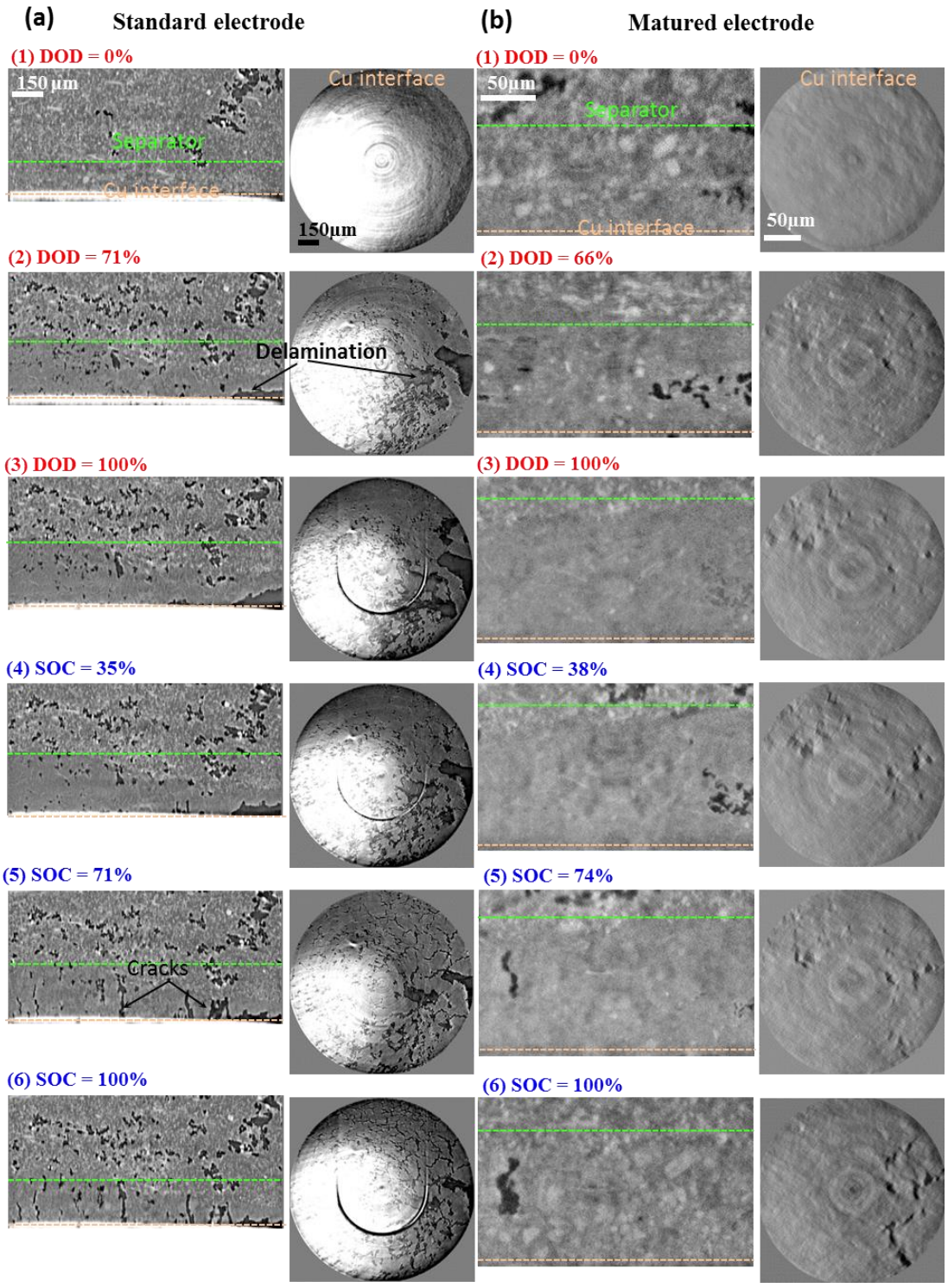

Figure S5. XRCT transversal images and lateral images in the electrode/current interface zone acquired at different DOD and SOC levels for the (a) standard electrode and (b) the matured electrode.

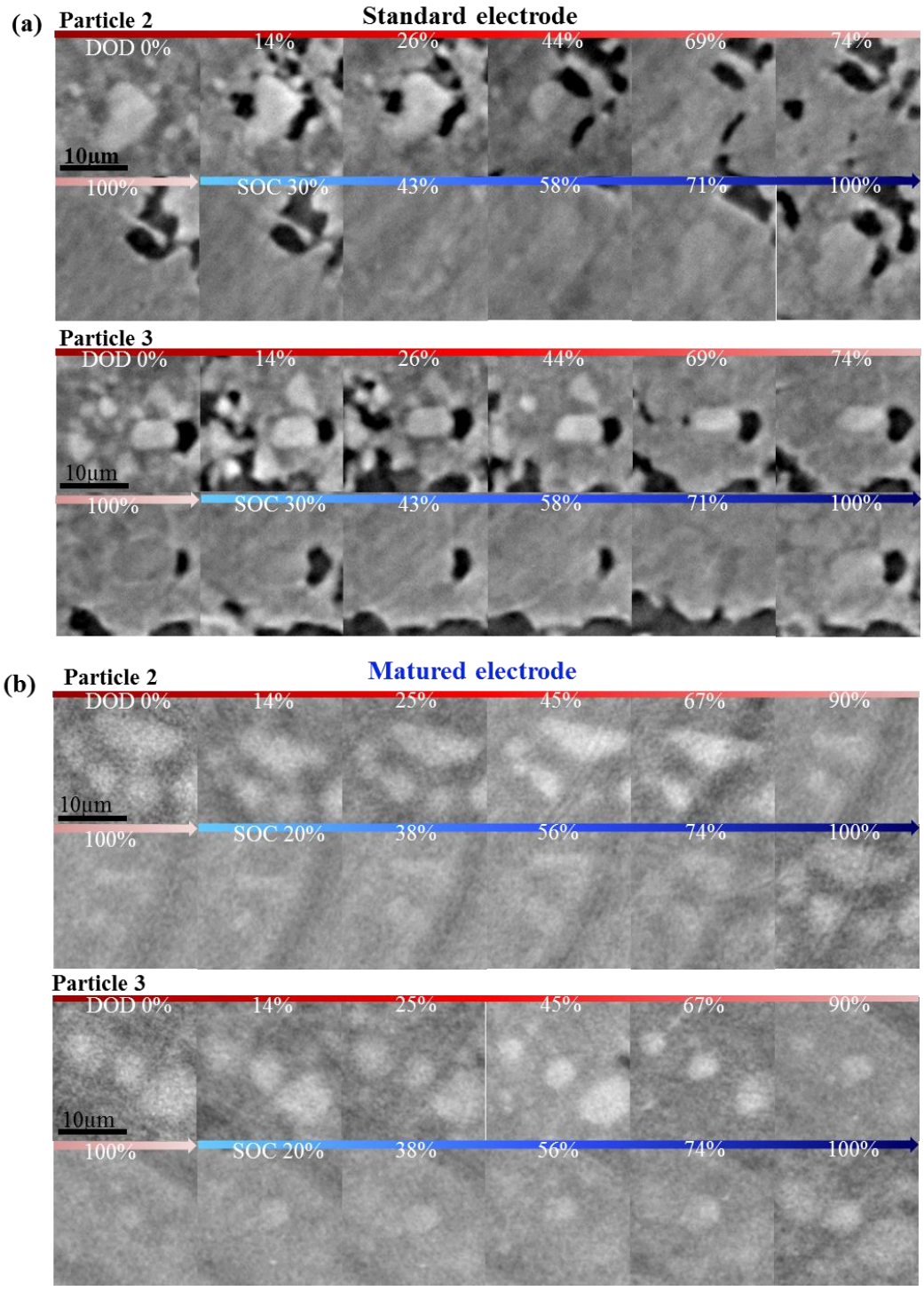

Figure S6. Evolution during the 1st cycle of XRCT lateral images focused on Si particles #2 and #3 for the (a) standard and (b) matured electrodes.

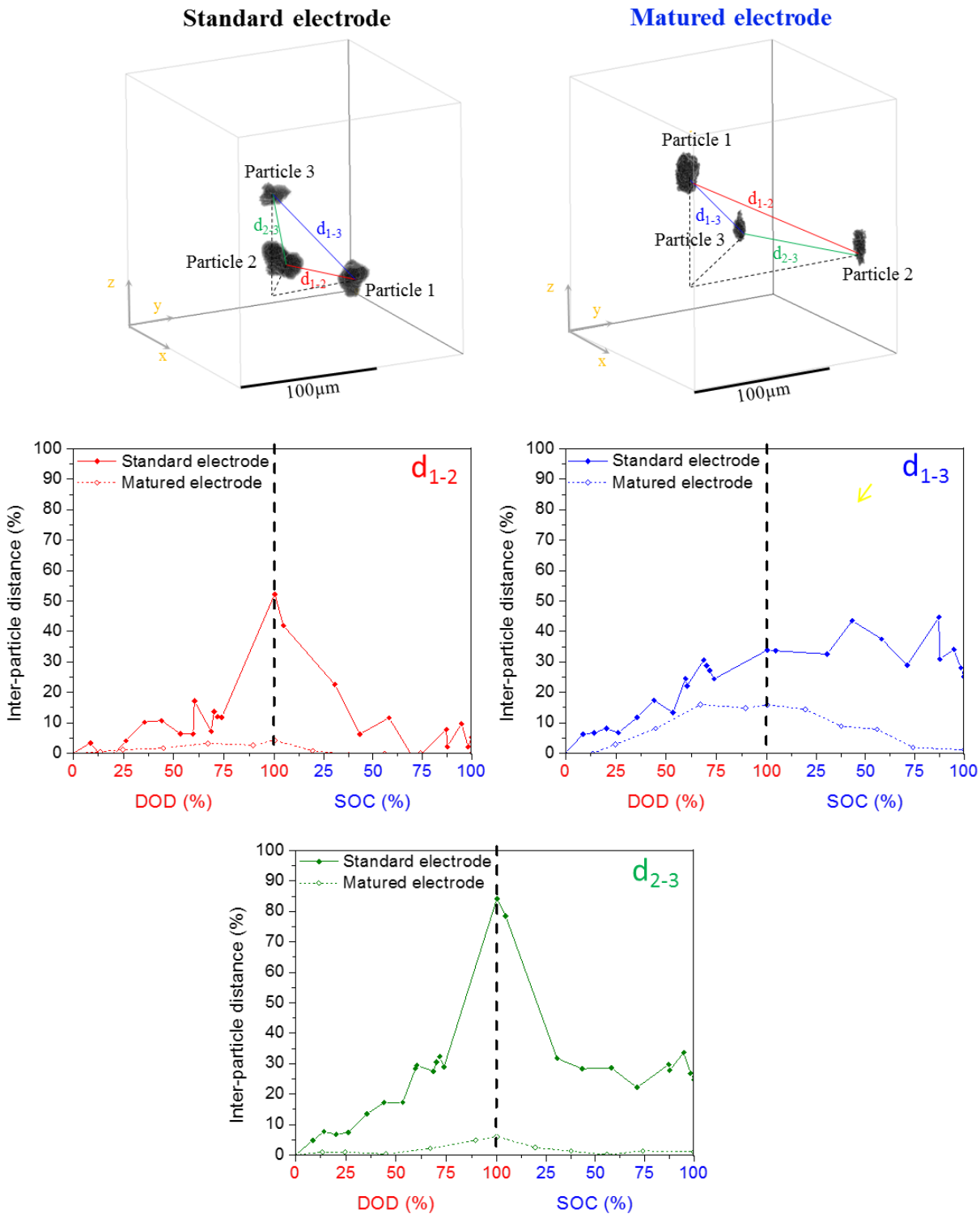

Figure S7. Evolution of the Si inter-particle distances $d_{1\text{-}2}$, $d_{1\text{-}3}$ and $d_{2\text{-}3}$ (expressed in relative variation) during the 1st cycle for the standard and matured electrodes

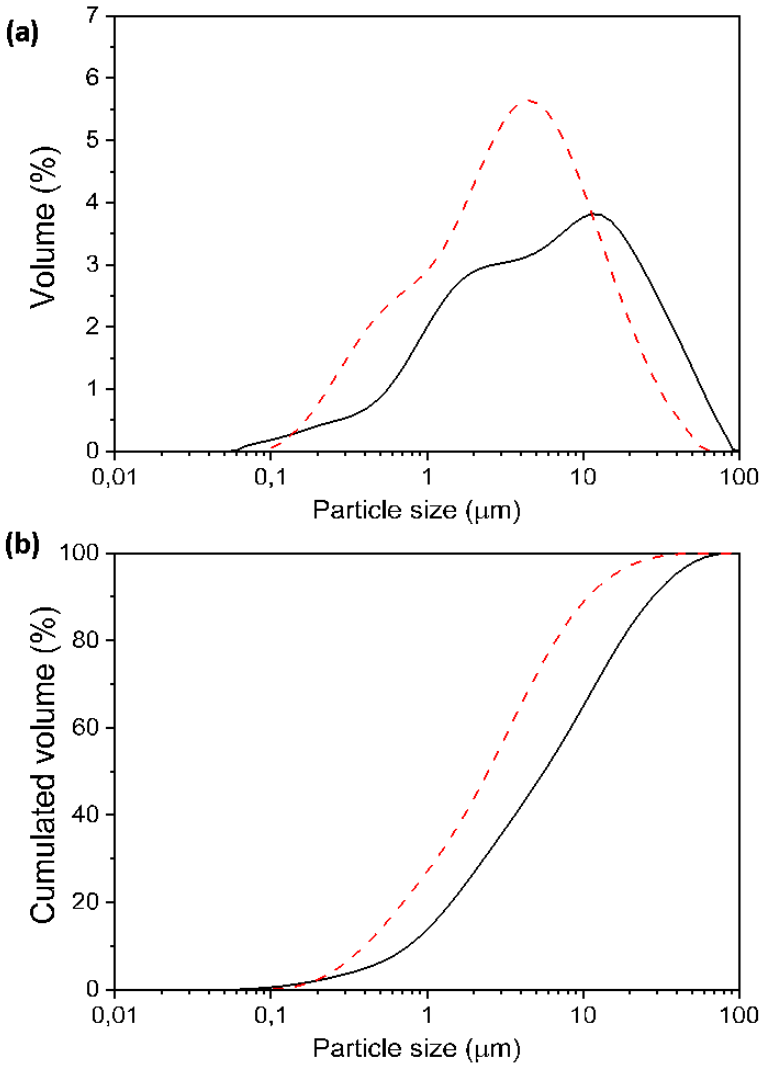

Figure S8. Particle size distribution curves in (a) vol. % and in (b) cumulated vol. % of the as-milled Si powder (black curves) and after a subsequent mixing for 1 h in water using a magnetic stirrer (red curves). Measurements were performed by laser scattering method using a Mastersizer 2000 Malvern analyser.

XRCT movies

1) Cracking dynamic for the standard electrode

Video 1: https://drive.google.com/open?id=1RvTW9Yl-xODVR_-rRp_Gep3m9kRxBSfi

2) Cracking dynamic for the matured electrode

Video 2: https://drive.google.com/open?id=13yL3TG_UvZigOTs0Je7wt-S3jHXtQXdO

3) Delamination dynamic for the standard electrode

Video 3 : https://drive.google.com/open?id=1AjwmsQFvKz7xjNeyyC4sn3m_aIZ19eQr

4) Delamination dynamic for the matured electrode

Video 4: https://drive.google.com/open?id=1BXku5pbDlOBndAiaUTja_JdxBxl7mi5h